

Recent trends and variability in the oceanic storage of dissolved inorganic carbon

L. Keppler^{1,2,3}, P. Landschützer^{4,2}, S.K. Lauvset⁵, N. Gruber⁶

¹Scripps Institution of Oceanography, University of California San Diego, La Jolla, CA, USA

²Max Planck Institute for Meteorology, Hamburg, Germany

³International Max Planck Research School on Earth System Modelling, Hamburg, Germany

⁴Flanders Marine Institute (VLIZ), Ostend, Belgium

⁵NORCE Norwegian Research Centre, Bjerknes Centre for Climate Research, Bergen, Norway

⁶Environmental Physics, Institute of Biogeochemistry and Pollutant Dynamics, ETH Zurich, Zurich,

Switzerland

Key Points:

- From 2004 through 2019, the global oceanic dissolved inorganic carbon (DIC) pool increased at an average rate of $3.2 \pm 0.7 \text{ Pg C yr}^{-1}$
- Most of this increase is associated with the uptake of anthropogenic CO_2 , while natural CO_2 is mostly redistributed within the ocean
- The interannual variability of DIC is largest in the tropical Pacific Ocean

Corresponding author: Lydia Keppler, lkeppler@ucsd.edu

This article has been accepted for publication and undergone full peer review but has not been through the copyediting, typesetting, pagination and proofreading process, which may lead to differences between this version and the [Version of Record](#). Please cite this article as [doi: 10.1029/2022GB007677](https://doi.org/10.1029/2022GB007677).

This article is protected by copyright. All rights reserved.

Abstract

Several methods have been developed to quantify the oceanic accumulation of anthropogenic carbon dioxide (CO_2) in response to rising atmospheric CO_2 . Yet, we still lack a corresponding estimate of the changes in the total oceanic dissolved inorganic carbon (DIC). In addition to the increase in anthropogenic CO_2 , changes in DIC also include alterations of natural CO_2 . Once integrated globally, changes in DIC reflect the net oceanic sink for atmospheric CO_2 , complementary to estimates of the air-sea CO_2 exchange based on surface measurements. Here, we extend the MOBO-DIC machine learning approach by Keppeler et al. (2020a) to estimate global monthly fields of DIC at 1° resolution over the top 1500 m from 2004 through 2019. We find that over these 16 years and extrapolated to cover the whole global ocean down to 4000 m, the oceanic DIC pool increased close to linearly at an average rate of $3.2 \pm 0.7 \text{ Pg C yr}^{-1}$. This trend is statistically indistinguishable from current estimates of the oceanic uptake of anthropogenic CO_2 over the same period. Thus, our study implies no detectable net loss or gain of natural CO_2 by the ocean, albeit the large uncertainties could be masking it. Our reconstructions suggest substantial internal redistributions of natural oceanic CO_2 , with a shift from the mid-latitudes to the tropics and from the surface to below $\sim 200 \text{ m}$. Such redistributions correspond with the Pacific Decadal Oscillation and the Atlantic Multidecadal Oscillation. The interannual variability of DIC is strongest in the tropical Western Pacific, consistent with the El Niño Southern Oscillation.

1 Introduction

The global oceanic dissolved inorganic carbon (DIC) pool is a powerful recorder of changes in the net exchange of carbon dioxide (CO_2) across the air-sea interface, i.e., the strength of the net oceanic carbon sink. This net sink is the sum of a flux of natural carbon (C_{nat}) that reflects the exchange driven by changes in solubility, ocean circulation, mixing, and biological processes, and the flux of anthropogenic carbon (C_{ant}) that corresponds to the anomalous flux of CO_2 driven by the human-induced rise in atmospheric CO_2 (McNeil & Mearns, 2013; Gruber et al., 2023). When integrated globally, the sources and sinks of natural CO_2 fluxes cancel each other out in a steady state as the ocean strives towards equilibrium with the overlaying atmosphere (Landschutzer et al., 2022). On the contrary, the observed increase in the net air-sea CO_2 exchange is caused by anthropogenic CO_2 emissions (Friedlingstein et al., 2022). An important exception is residual outgassing that reflects the balance between the input of carbon by rivers and the deposition of carbon on the seafloor (Sarmiento & Sundquist, 1992; Regnier et al., 2022). As long as this balance is maintained, this latter (i.e., natural) component does not leave an imprint on changes in DIC, so that changes in this pool are then directly attributable to the ocean interior accumulation or loss of both natural and anthropogenic CO_2 .

Knowing the magnitude of the net oceanic sink for CO_2 is crucial for closing the global carbon budget and its anthropogenic perturbation (Sarmiento & Gruber, 2002; Friedlingstein et al., 2022). The need is heightened by efforts such as the United Nations' global stocktake efforts (<https://unfccc.int/topics/science/workstreams/global-stocktake>), which require a more refined estimate of the changing ocean carbon content, connecting the surface and interior ocean, and demonstrating the total changes in DIC, as well as its spatial distribution. Finally, better global-scale constraints on the changes in oceanic DIC are of great interest to better document the progression of ocean acidification and better establish the connection between changes in seawater chemistry and biological impacts (Doney et al., 2009; Orr et al., 2005; Feely et al., 2004).

In terms of observations, the net oceanic CO_2 sink is at present primarily determined using measurements of the surface ocean partial pressure of CO_2 ($p\text{CO}_2$), which are mapped to the globe using various data interpolation methods (Landschutzer et al., 2014; Rdenbeck

68 et al., 2015; Fay et al., 2021; Gregor & Gruber, 2021). The mapped $p\text{CO}_2$ is then used,
69 in combination with the atmospheric $p\text{CO}_2$ and the gas transfer velocity, to estimate the
70 air-sea CO_2 flux. However, this approach is subject to various uncertainties, such as data
71 sparsity (Fay & McKinley, 2013), an ill-constrained gas transfer coefficient (Wanninkhof
72 et al., 2009; Roobaert et al., 2019), and a potential offset in the $p\text{CO}_2$ measurements as
73 they are not directly taken at the cool skin surface (Watson et al., 2020). Furthermore,
74 the steady-state outgassing of river-derived carbon needs to be subtracted from the inferred
75 flux to obtain the anthropogenic flux relevant to the global carbon budget. Estimates for
76 this riverine flux range from $0.23 \text{ Pg C yr}^{-1}$ (Lacroix et al., 2020) and $0.45 \pm 0.18 \text{ Pg C yr}^{-1}$
77 (Jacobson et al., 2007) to $0.78 \pm 0.41 \text{ Pg C yr}^{-1}$ (Resplandy et al., 2018), with the most
78 recent review by Regnier et al. (2022) suggesting a value of $0.65 \pm 0.3 \text{ Pg C yr}^{-1}$. This range
79 and the associated uncertainties add further uncertainty to the $p\text{CO}_2$ derived estimates of
80 the net carbon uptake by the global ocean.

81 Confidence in quantifying this net uptake could be strengthened if constrained
82 independently through the direct determination of changes in the global ocean DIC
83 content. Nevertheless, this is a challenging task, owing to the sparsity of observations, the
84 substantial background DIC pool of $\sim 37,000 \text{ Pg C}$ (Keppler et al., 2020b), and the many
85 physical and biological processes that govern the distribution of DIC in the ocean
86 (Sarmiento & Gruber, 2006). A very successful approach to overcome this challenge has
87 been to only focus on the interior ocean's accumulation of the C_{ant} component (Wallace,
88 1995; Tanhua et al., 2007). Under the assumption that the ocean is in a near steady state,
89 several methods have been developed to determine the changes in C_{ant} either from single
90 surveys of DIC (Brewer, 1978; Chen & Millero, 1979; Gruber et al., 1996), or from repeat
91 hydrography programs (Friis et al., 2005; Clement & Gruber, 2018; Carter et al., 2019).
92 The application of these methods has permitted the oceanographic community to quantify
93 the increase in the C_{ant} inventory, both since preindustrial times (Gruber, 1998; Sabine et
94 al., 1999) and for the past few decades (Friis et al., 2005; Wanninkhof et al., 2010; Carter
95 et al., 2019), with the global studies providing invaluable constraints for the global budget
96 of C_{ant} (Sabine et al., 2004; Gruber et al., 2019).

97 Although these global C_{ant} estimates have proven to be extremely valuable for
98 constraining the global carbon budget and hence the fate of the emitted anthropogenic
99 CO_2 , they have not been able to fully address whether the steady-state assumption or the
100 assumption of a small C_{nat} signal is justified. Questions were raised early on, especially in
101 the context of ocean warming (Keeling, 2005; Sabine & Gruber, 2005), which many models
102 suggest will lead to a loss of CO_2 from the ocean (Joos et al., 1999; Sarmiento et al., 1998;
103 Matear & Hirst, 1999). Later, using a combination of different model and
104 observation-based methods, McNeil and Matear (2013) invoked the presence of a
105 decadal-scale outgassing signal of C_{nat} , but without being able to support this conjecture
106 with direct observations. Dedicated modeling studies also suggest that the ocean might
107 have lost C_{nat} in recent decades, e.g., in response to the trends in the Southern Annular
108 Mode (Le Qur et al., 2007; Lenton & Matear, 2007; Zickfeld et al., 2007; Hauck et al.,
109 2013; Lovenduski et al., 2008, 2007). In their global study on the increase in anthropogenic
110 CO_2 between 1994 and 2007, Gruber et al. (2019) speculated that perhaps as much as
111 5 Pg C of C_{nat} might have been lost from the ocean over this period. A recent review by
112 Gruber et al. (2023) further assessed the role of the non-steady state and the associated
113 potential loss of C_{nat} . Conversely, enhanced lateral transport of natural carbon from the
114 land could yield a gain of C_{nat} in the ocean (Regnier et al., 2022). Similarly, changes in
115 the circulation or biological productivity could cause an anomalous uptake or release of
116 CO_2 from the atmosphere, altering the total stock of C_{nat} .

117 As the arguments for potential changes in C_{nat} accumulate, the need to constrain
118 the changes in the total DIC pool increases, as this permits to assess the changes in both
119 natural and anthropogenic CO_2 . When doing so, one needs to also consider that even if
120 the global-scale changes in the natural CO_2 pool might be small, this pool is subject to

121 strong redistributions within the ocean, associated with changes in circulation, shifts in
122 ocean fronts, and changes in biological productivity, causing locally large changes in DIC
123 (Clement & Gruber, 2018). Such changes are commonly seen when comparing the DIC
124 distributions between two occupations of a particular hydrographic section (Wanninkhof
125 et al., 2010; Carter et al., 2019). They are also expected in the context of interannual
126 variability, especially in regions with large vertical undulations of the thermocline, and
127 hence also the “carbocline,” i.e., the strong vertical gradient in DIC. Such redistributions
128 of DIC within the ocean not only pose a challenge for the detection of global-scale changes
129 in the DIC pool, but they also potentially threaten organisms, as spatial redistributions of
130 DIC might cause more rapid local changes in ocean acidification and, perhaps, a more rapid
131 reaching of critical thresholds (McNeil & Sasse, 2016).

132 Currently, no sensor technology exists that can operationally measure DIC in situ.
133 Thus, we must rely on physical seawater samples collected and analyzed during ship-based
134 surveys and programs (Talley et al., 2016; Bates et al., 2014), strongly limiting the coverage
135 and the sampling frequency. Most of these DIC measurements and the associated ancillary
136 data are compiled and subjected to secondary quality control by the Global Ocean Data
137 Analysis Project (GLODAP; Olsen et al. (2016); Key et al. (2004)). A recent version
138 (GLODAPv2.2021) contains over one million measurements from across the global ocean,
139 spanning measurements from 1972 to 2020 (Lauvset et al., 2021). Most of the measurements
140 contained within GLODAP stem from repeat hydrography programs, where the same set
141 of stations along long lines are revisited at roughly decadal intervals (Talley et al., 2016).
142 In addition to GLODAP, some long-term time-series stations provide information on the
143 temporal variability in the interior ocean at a few locations, including the Hawaii Ocean
144 Timeseries (HOT; Dore et al. (2009)) and the Bermuda Atlantic Timeseries Study (BATS;
145 Bates et al. (2014)). More recently, Argo floats equipped with biogeochemical (BGC) sensors
146 that measure pH, salinity, and other variables, supplement the ship data. Using these float
147 measurements and some empirical relationships to infer alkalinity, DIC can be estimated
148 (Carter et al., 2018; van Heuven et al., 2011). However, this method has much larger
149 uncertainties than the ship data (Bittig et al., 2018), and to date, the available BGC-Argo
150 float data are largely limited to the Southern Ocean, as part of the Southern Ocean Carbon
151 and Climate Observations and Modelling project (SOCCOM; Talley et al. (2019)), while
152 the global ocean BGC-Argo array is still in its early stages (Bittig et al., 2019).

153 In parallel to the efforts in combining and unifying carbon cycle observations (Olsen
154 et al., 2016; Bakker et al., 2016), a second branch related to big data analysis based on
155 machine learning has emerged. Keppler et al. (2020b) adopted a cluster-regression approach
156 previously applied to reconstruct the air-sea CO₂ exchange (Landschutzer et al., 2013, 2014)
157 and extended it to map a monthly climatology of DIC in the upper 2000 m of the near-
158 global ocean, i.e., Mapped Observation-Based Oceanic DIC (MOBO-DIC; Keppler et al.
159 (2020a)). Similarly, Broulln et al. (2020) developed a single-step machine learning approach
160 to map the monthly climatology of interior DIC at a global scale. In addition, a recent
161 study has mapped out the temporal evolution of DIC globally (Gregor & Gruber, 2021),
162 but this approach was limited to the documentation of variations at the sea surface. These
163 studies revealed the feasibility of reconstructing the DIC content from observations at the
164 global scale. In addition, using CMIP6 models and synthetic Argo data, Turner et al. (2022)
165 demonstrated very recently that interior temperature and salinity data are well suited to
166 reconstruct interior DIC fields and their variability. However, they have not yet mapped
167 the interior ocean DIC with real-world Argo observations. Further, Sharp et al. (2022)
168 successfully mapped monthly fields of interior ocean dissolved oxygen at a global scale, using
169 a machine learning approach. However, mapped estimates of interior observation-based
170 DIC remain limited to seasonal climatologies (Keppler et al., 2020b; Broulln et al., 2020)
171 or the surface (Gregor & Gruber, 2021), and reconstructions of the trend and interannual
172 variability of the upper ocean total DIC at the global scale based on direct observations are
173 still lacking.

174 To fill this gap, we use the MOBO-DIC approach and extend the monthly climatology of
175 DIC by Keppler et al. (2020b) to resolve monthly global DIC fields from 2004 through 2019
176 (i.e., January 2004 through December 2019). The temporal extent of our reconstructions
177 is primarily determined by the availability of temperature and salinity fields from the Argo
178 program that we use as key predictors. Our new DIC product is mapped at a monthly
179 resolution on a $1^\circ \times 1^\circ$ grid, from 65°N to 65°S , and reaching 80°N in the Atlantic (see
180 Supporting Information Fig. S1), extending from 2.5 m to 1500 m depth. Subsequently,
181 we investigate the trend and interannual variability of the interior oceanic DIC at a global
182 scale and put these changes into the context of the ongoing accumulation of anthropogenic
183 CO_2 in the ocean's interior and from this, infer the changes in the natural CO_2 pool.

184 2 Data and Methods

185 2.1 Cluster-regression

186 We adopt the two-step neural network MOBO-DIC approach introduced by Keppler
187 et al. (2020b) to map the sparse DIC observations to the (near) global ocean at monthly
188 resolution for the period January 2004 through December 2019. Here, we present a
189 summary of the most important features and the main changes compared to the
190 climatological approach taken by Keppler et al. (2020b). Our approach first clusters the
191 ocean into regions of similar properties using self-organizing maps (SOM) and then applies
192 a feed-forward neural network (FFN) in each cluster to reconstruct a physical relationship
193 between a set of driver variables and the target DIC data. This cluster-regression
194 approach does not require information about the measurement location, a feature that
195 separates it from many other mapping approaches (Sasse et al., 2013; Gregor et al., 2017;
196 Bittig et al., 2018; Broulln et al., 2019, 2020). Thus, our regression method is solely based
197 on the physical and biogeochemical relations between the predictor and target variables.
198 Not using the measurement location as a predictor permits our method to benefit from
199 information obtained in other places within each cluster, where predictor and target data
200 are similarly related. Due to data availability (silicic acid and nitrate are only available in
201 the upper 500 m) and the presence of different processes near the surface and below, we
202 run the method separately for two depth slabs: from 2.5 m to 500 m and from 500 m to
203 1500 m. We take the mean of the two estimates at 500 m to minimize boundary problems
204 between the two depth slabs. This approach does not eliminate all discontinuities, but
205 they are well within the uncertainty limits of the method.

206 In the first step, we use a SOM, i.e., a type of unsupervised machine learning, to
207 determine clusters. Following Keppler et al. (2020b), we use six clusters in the upper 500 m
208 and four between 500 m and 1500 m. We tested various set-ups, including different numbers
209 of clusters, and found that this number of clusters leads to the smallest overall error in the
210 DIC reconstruction. To avoid boundary problems inherent in cluster-regression approaches,
211 we adjust the original method by creating an ensemble of SOM clusters, following the
212 approach introduced by Gregor and Gruber (2021). To this end, we performed the SOM-
213 step three times, where the DIC input has a different weight ranging from 2 to 4 in each run.
214 The resulting SOM clusters vary mostly around the boundaries (see Supporting Information
215 Fig. S2). In the second step, we run an FFN for each SOM cluster. Our FFN network
216 architecture consists of 8 neurons in the hidden layer of the FFN, as this setup results in
217 the most robust output based on a comparison between the mapped output and the original
218 training data.

219 To avoid overfitting, we use 80% of the input data to train the network and the
220 remaining 20% for internal cross-validation. As the training and validation data are
221 separated randomly, the output from the FFN is slightly different each time it is run. For
222 each SOM setup, we run the FFN five times, where each time, the data is separated
223 differently into training and validation data to create an ensemble of outputs. Thus, our
224 ensemble comprises 15 members (three SOM setups, each with five FFN runs). The final

225 reported data are the mean across the ensemble, and the standard deviation across the
226 ensemble represents the uncertainty linked to the weighting of the SOM clusters and the
227 random assignment of training and validation data (hereafter referred to as prediction
228 uncertainty, see Supporting Information Fig. S3). We smooth the ensemble mean fields at
229 each depth level by taking the running mean with a window size of three grid cells in each
230 horizontal direction (latitude and longitude) and the temporal dimension.

231 Some runs produced outputs with unlikely values, e.g., considerably larger or smaller
232 than the measured variables in GLODAP. We attribute this to the random assignment of
233 training and validation data, where some data subsets are unsuitable for training. Such runs
234 with unlikely values occurred both with the GLODAP training data and with synthetic data,
235 so it cannot be attributed to noise in the observations. We have tried many different setups
236 of the network to eliminate this issue. However, with the current training data, we were
237 unable to resolve it. Thus, when an output results in values that are more than 5 standard
238 deviations larger or smaller than the observed data in GLODAP (i.e., outside of the range
239 1639 to 2575 $\mu\text{mol kg}^{-1}$ and 1898 to 2629 $\mu\text{mol kg}^{-1}$, for the upper and lower depth slab,
240 respectively), the entire ensemble member was discarded and re-run with the same setup,
241 but with a different sub-set of training data. We trust that removing the runs with unlikely
242 values, in addition to the bootstrapping approach, yields a robust estimate.

243 2.2 Data and Domain

244 As input to the SOM, we use monthly mapped fields of temperature and salinity based
245 on Argo float measurements (Roemmich & Gilson, 2009) and an annual-mean climatology
246 of DIC (Lauvset et al., 2016). We weigh the DIC input stronger than the physical predictors
247 so that the clusters largely represent the climatological mean DIC and, to a lesser extent,
248 the physical water masses, following Landschtzer et al. (2013).

249 For the FFN step, we use the ship measurements of DIC from GLODAPv2.2021 between
250 January 2004 and December 2019 (Lauvset et al., 2021) as the target data. We only retain
251 GLODAP data with a WOCE quality control of 0 or 2 and a secondary quality control flag
252 of 1. As predictors, we use the same Argo-based temperature and salinity fields that we
253 used during the SOM step. In addition, we use monthly climatologies of mapped dissolved
254 oxygen, nitrate, and silicic acid from the World Ocean Atlas 2018 (WOA18; Boyer et al.
255 (2018)). These climatologies are based on ship measurements from 1955 through 2017 and
256 were interpolated to the global ocean using optimal interpolation. As the nitrate and silicic
257 acid from WOA only extend until 500 m, they were not used as predictors in the deeper
258 slab, while dissolved oxygen extends to 1500 m in WOA and is thus a predictor variable in
259 both depth slabs. Deviating from the approach taken to produce the monthly climatology
260 of MOBO-DIC (Keppler et al., 2020b), we use atmospheric pCO_2 as an additional predictor
261 in the upper depth slab (0 to 500 m) to be able to represent the long-term trend in the
262 atmospheric CO_2 concentration. Atmospheric pCO_2 at each grid cell was computed from the
263 GlobalView marine boundary layer product of the mole fraction of CO_2 ($x\text{CO}_2$; GlobalView-
264 CO_2 (2011)) and converted to pCO_2 following Landschtzer et al. (2013). In the deeper slab
265 below 500 m, we use Julian days as a predictor to represent any long-term trend in the
266 data. We tested various set-ups where we use latitude and longitude (in the form of $\sin(\text{lon})$
267 and $\cos(\text{lon})$), and depth as input variables, and found that the inclusion of this spatial
268 information in the predictors did not improve our DIC reconstructions. Thus, the predictors
269 between the surface and 500 m are temperature, salinity, dissolved oxygen, nitrate, silicic
270 acid, and atmospheric pCO_2 . Between 500 m and 1500 m, we use temperature, salinity,
271 dissolved oxygen, and Julian day as predictors. A more detailed discussion on the choice of
272 predictors can be found in Keppler et al. (2020b).

273 Note that we use the mapped monthly mean fields as predictors, as opposed to the
274 co-measured data from GLODAP during the training step of the FFN. We tested both
275 approaches but found the results were very noisy when using the co-measured data as

276 predictors. This noisy output may be partially caused by the WOA monthly gridded fields
277 being smoother than the point measurements in GLODAP. Furthermore, using the co-
278 measured predictors leads to a substantial loss of training data, as in $\sim 60,000$ data points
279 out of $\sim 440,000$ (i.e., $\sim 14\%$), the training data do not have usable co-measured predictors.

280 The availability of the data limits the domain and resolution of our mapping approach.
281 For example, we limit the vertical extent of the multi-year product here to 1500 m (as
282 opposed to 2000 m used for the MOBO-DIC climatology) as the DIC observations are
283 very sparse below 1500 m and only temperature and salinity are available as physical or
284 biogeochemical predictors there. This lack of predictors below 1500 m prevents a robust
285 estimate of the DIC variations and trends at these depths. Temporally and spatially, the
286 limits tend to be set by the predictor data. The Argo-based data products used here extend
287 from 65°N to 65°S globally, to 80°N in the Atlantic Ocean, with shallow coastal regions
288 being masked, marking the horizontal extent of our domain. As the mapped Argo-dataset
289 starts in 2004, and GLODAPv2.2021 includes cruise data until January 2020, the temporal
290 extent of MOBO-DIC is from January 2004 through December 2019.

291 All predictors have a monthly resolution on $1^\circ \times 1^\circ$ grids, and we interpolate them onto
292 28 uneven depth levels between 2.5 m and 1500 m. Note that due to an update to the Argo
293 data, the domain of this study is slightly larger than in the monthly climatology of MOBO-
294 DIC (Keppler et al., 2020b): it extends further north in the Atlantic (until 80°N instead of
295 65°N), and some more coastal and shallow regions are included (see Supporting Information
296 Fig. S1). As the domain covers most of the global ocean, we refer to our domain as global
297 in-text but want to note that it is technically only near-global.

298 **2.3 Calculation of the trend and inventory changes**

299 We estimate the trend in DIC over our period based on the slope of a linear regression
300 of the deseasonalized DIC at each grid cell. The data were deseasonalized by applying a
301 12-month running mean at each grid cell. To calculate the trends in the inventories, we first
302 normalize DIC for salinity (hereafter sDIC) to remove any effects from potential changes in
303 the salinity, following Friis et al. (2003). For this normalization, we use the same monthly
304 Argo-based salinity product as above (Roemmich & Gilson, 2009), using the temporal mean
305 salinity from 2004 through 2019 at each grid cell as reference salinity. We convert sDIC from
306 gravimetric (unit: $\mu\text{mol kg}^{-1}$) to volumetric (unit: $\mu\text{mol m}^{-3}$), and then vertically integrate
307 the volumetric trend in the whole domain (upper 1500 m). To estimate the uncertainty in the
308 trend, we calculate it with each of the 15 ensemble members and take the standard deviation
309 range as the uncertainty range. Note that the uncertainty of the trend only includes the
310 ensemble spread (i.e., the prediction uncertainty) and does not consider other sources of
311 error, for example, those associated with measurements or representation uncertainty. We
312 trust that there should not be a trend in measurement or representation uncertainty in
313 the data, yielding a robust estimate of the overall trend uncertainty. We then conduct an
314 upscaling to estimate the global changes in sDIC that include regions beyond our domain,
315 i.e., the high latitudes, coastal regions, and below 1500 m (see Supporting Information
316 Section S3).

317 **2.4 Comparison with C_{ant}**

318 We compare the trend in MOBO-DIC with an estimate of the change in anthropogenic
319 CO_2 (ΔC_{ant}). For this comparison, we use two estimates of C_{ant} and scale them to our
320 study period. The two estimates are (i) the total change in C_{ant} between 1800 and 2007
321 and (ii) the change in C_{ant} between 1994 and 2007. The former is estimated by adding the
322 total C_{ant} up to 1994 estimated by Sabine et al. (2004) to the change in C_{ant} between 1994
323 and 2007 estimated by Gruber et al. (2019). For the latter, we use the ΔC_{ant} by Gruber et
324 al. (2019).

To scale C_{ant} to our period, we apply the transient steady-state approach described by Mikaloff Fletcher et al. (2006) and Gruber et al. (2019), which relies on the assumption that the change in C_{ant} scales with the change in atmospheric CO_2 :

$$\Delta C_{ant}^{t_3-t_2} = \alpha(t_0, t_1, t_2, t_3) \cdot \Delta C_{ant}^{t_1-t_0} \quad (1)$$

where t_0 and t_1 are the bounds of the periods used to determine ΔC_{ant} (either 1800 through 2006 or 1994 through 2006) and t_2 and t_3 bound the period to which the scaling should be applied to (here: 2004 through 2019). The scaling factor α is specific for each pair of periods, i.e., is a function of t_0, t_1, t_2 , and t_3 , and can be estimated from the relative changes in atmospheric CO_2 , also considering changes in the Revelle factor (Sarmiento et al., 1995) and the changes in the air-sea disequilibrium (Gruber et al., 1996; Matsumoto & Gruber, 2005):

$$\alpha(t_0, t_1, t_2, t_3) = \frac{\Delta_t p\text{CO}_2^{atm}(t_3 - t_2)}{\Delta_t p\text{CO}_2^{atm}(t_1 - t_0)} \cdot \frac{\xi(t_2..t_3)}{\xi(t_0..t_1)} \cdot \frac{\gamma(t_2..t_3)}{\gamma(t_0..t_1)} \quad (2)$$

where the first factor on the right-hand side is the relative change in atmospheric CO_2 , the second factor is the relative change in the disequilibrium ξ , and the third factor is the relative change in the Revelle factor γ .

In the first case, i.e., for the base period 1800 through 2006, inserting the observed values in atmospheric CO_2 in the respective years ($t_0 = 1800$, 280 ppm; $t_1 = 2006$, 381 ppm; $t_2 = 2004$; 377 ppm, $t_3 = 2019$, 410 ppm) gives a value of 0.33 for the first factor on the right-hand side of Eq. 2. For the disequilibrium, we take the same estimate Gruber et al. (2019) used when scaling from 1800 through 1993 to 1994 through 2006. They estimated a change in the disequilibrium of about 6 μatm between 1800 and 1994, and about 3 μatm between 1994 and 2007, yielding a ratio of 0.94. Similarly, we also take the estimate by Gruber et al. (2019) of 0.94 for the third factor, i.e., the ratio of the Revelle factors. Entering these three ratios, we obtain an overall scaling factor α of 0.29 ($0.33 \cdot 0.94 \cdot 0.94$) when comparing the period 1800 to 2007 with the period from 2004 through 2019.

In the second case, the base period for the scaling factor goes from 1994 (t_0 , 358 ppm) through 2006 (t_1 , 381 ppm), yielding a relative change in atmospheric CO_2 of 1.45 compared to the period 2004 (t_2 , 377 ppm) through 2019 (t_3 , 410 ppm). As the two periods are largely overlapping in this case, we assume that the ratio of the disequilibrium and the ratio of the Revelle factors are very close to 1 and thus set their values to 1, yielding an overall scaling factor α of 1.45 when comparing the period 1994 to 2007 with the period from 2004 through 2019.

This scaling is based on many assumptions, especially the assumption of a transient steady-state. While the large-scale distribution of C_{ant} has been demonstrated to follow this prediction rather closely, Gruber et al. (2019) pointed out that the reconstructed distribution of the change in C_{ant} between 1994 and 2007 differs in a few places considerably from that reconstructed for the period up to 1994. In particular, they found a meridional shift in the accumulation within the Atlantic Ocean, with a reduction in the North Atlantic storage being compensated by an increase in the temperate latitudes of the South Atlantic. Using two different base periods, we attempt to quantify the potential impact of such changes on our conclusions. Direct estimates of the accumulation of C_{ant} over the same period as analyzed here would be preferable to our scaling approach but are not published to date.

3 Uncertainty Assessment

Our method fills very substantial gaps in space and time (see Supporting Information Fig. S4). The GLODAP observations of DIC cover even less of the ocean in horizontal

space and time than the surface fCO₂ measurements in the SOCAT database that are used to construct surface ocean flux products (Landschutzer et al., 2014; Gregor & Gruber, 2021; Rdenbeck et al., 2015), i.e., SOCAT only covers approximately 3% of 1°x1° grid cells for any given month across the surface ocean in the 2010s (Gruber et al., 2023). Although GLODAP contains more data points by containing the vertical dimension, i.e., interior ocean data, we still have to fill substantial gaps at each depth level. In each year from 2004 through 2019, we have on average 30±9 (mean±1 standard deviation) observations per depth bin. Assuming that this observation was representative of a 2°x2° grid at each depth level, would mean that only about 0.3% of the global ocean was observed for any given month, requiring that the other 99.7% are filled through our statistical gap-filling methodology. Thus, we emphasize that users keep the different uncertainties in mind when using our product and interpreting our results. Here, we summarize the different sources of uncertainty in our analysis.

3.1 Calculation of the overall uncertainty

We identify three main sources of uncertainties that contribute to the total uncertainty of our DIC estimate, following Gregor and Gruber (2021): the uncertainties linked to the measurements (M), the representation (R), and the prediction (P). The overall uncertainty of our DIC estimate (DIC_{err}) can then be estimated with standard error propagation:

$$DIC_{err} = \sqrt{M^2 + R^2 + P^2} \quad (3)$$

The uncertainty M linked to the measurements stems from sampling errors and imprecisions in the measurement system. While GLODAP currently does not report measurement uncertainties, they include a measure of spatial consistency based on inter-cruise comparisons, which amounts to 2.4 $\mu\text{mol kg}^{-1}$ for DIC (Lauvset et al., 2021). We assume that this uncertainty is the same at all grid points, which is likely an overestimation at some points and an underestimation at others.

The representation uncertainty R results from the fact that the discrete measurements in GLODAPv2.2021 that are used as target data to train the network are taken at one point in time and space and thus might not represent the true monthly mean of the 1°x1° grid cell and the depth bin it falls in. Especially problematic are regions where the spatiotemporal variability is high and the number of observations in a grid cell and depth bin is low. It is not straightforward to quantify the representation error as this requires full knowledge of the spatiotemporal variability of DIC. Gregor and Gruber (2021) estimated the representation error of total alkalinity of about 16 $\mu\text{mol kg}^{-1}$ at the sea surface of the open ocean. As the density and spatial distribution of total alkalinity and DIC measurements in GLODAP are similar, and regions with high spatiotemporal variability in total alkalinity tend to be regions of high variability in DIC as well, we adopt this estimate for all grid cells and depth bins. We recognize that alkalinity tends to be less variable than DIC, especially near the surface. In addition, the representation error is expected to be larger near the coast than in the open ocean due to more variability near the coasts and is also expected to decrease with depth (Torres et al., 2021), adding some uncertainty to our uncertainty estimate. Overall, we expect that R might be underestimated near the surface and the coast and overestimated at depth.

The prediction uncertainty P represents how well our method can map DIC in time and space. We take the standard deviation across the 15-member ensemble of our bootstrapping approach as our estimate of the prediction error. The differences in the ensemble members are linked to both the ensemble of SOM clusters and the different subsets of training and validation data, as described in Section 2.1. We note that our approach to quantify the prediction uncertainties only considers the spread induced by variations of the method and not the inherent uncertainty of the method itself. Thus, our approach may underestimate the potential errors stemming from the very limited

416 time-space distribution of the available data. As this error is difficult to quantify, we rely
417 on our evaluations with independent observations, previous mapped estimates, and
418 synthetic data (Section 4). The global mean prediction uncertainty is $7 \mu\text{mol kg}^{-1}$, but
419 with a large spread. We find the highest prediction error in the northern Indian Ocean (up
420 to $\sim 80 \mu\text{mol kg}^{-1}$), where the observations are particularly sparse and where our estimate
421 is heavily extrapolated (Supporting Information Fig. S3). Such large local uncertainties
422 illustrate that our approach can reconstruct global fields, but care must be taken when
423 evaluating regional changes, as the uncertainties on a regional level are quite high.
424 Combining the three uncertainty contributions (Eq. 3) yields an overall global mean
425 uncertainty of $18 \mu\text{mol kg}^{-1}$.

426 3.2 Quality of fit

427 During our mapping approach, we estimate the target data at all grid points. Thus,
428 unlike in an interpolation, there is a difference between the target data (i.e.,
429 GLODAPv2.2021) and the mapped estimate (i.e., MOBO-DIC). In Supporting
430 Information Fig. S4, we present these residuals to get a better handle on the quality of our
431 fits. This analysis intends to examine if there are any systematic offsets in different regions
432 or depth levels. It also highlights the magnitude of the differences between the training
433 data and MOBO-DIC. We find that there is no systematic under- or overestimation
434 compared to the training data, and the global mean bias cancels out to be 0, while the
435 global mean root mean square difference (RMSD) is $16 \mu\text{mol kg}^{-1}$ (see Table 1 and
436 Supporting Information Fig. S4), slightly less than our global mean uncertainty of
437 $18 \mu\text{mol kg}^{-1}$.

438 4 Evaluation

439 We evaluate the quality of the mapped MOBO-DIC product with various independent
440 observations and using a synthetic dataset derived from a model for which we know the true
441 value. Independence means here that these data were not used for the training of MOBO-
442 DIC (see Table 1 in the Main Text for a summary and Supporting Information Sections S5
443 and S6 and Figs. S5-S12 for a more in-depth analysis of the evaluation).

444 To evaluate our method with the synthetic data, we subsample the simulated DIC in
445 the biogeochemical component of the Ocean General Circulation Model HAMOCC (Ilyina
446 et al., 2013; Mauritsen et al., 2019) when and where we have observations in
447 GLODAPv2.2021. These synthetic data are pseudo-observations from the HAMOCC
448 model and not real observations. For the oxygen and nutrient fields that we use as
449 predictors, we use the monthly climatologies of these simulated variables, to be consistent
450 with our method using real observations. We then run our MOBO-DIC method with these
451 synthetic data to reconstruct the simulated DIC fields. We can then compare our
452 reconstructed fields with the actual DIC in HAMOCC.

453 For the observations, we use three different sources: First, we use a suite of mapped
454 DIC climatologies, all of which are based on GLODAP data (Lauvset et al., 2016; Kepler
455 et al., 2020b; Broulln et al., 2020). Second, we compare MOBO-DIC with observations from
456 time-series stations and biogeochemical Argo floats. Third, we use the mapped surface DIC
457 product contained in OceanSODA-ETHZ (Gregor & Gruber, 2021), allowing us to compare
458 the monthly $1^\circ \times 1^\circ$ fields at the surface when and where the two datasets overlap (January
459 2004 to December 2018).

460 We first evaluate the climatological mean, then the trend, and the interannual
461 variability, for each of these evaluation data where the temporal resolution allows. Note
462 that we use DIC and not sDIC in the evaluation with observations, as salinity is not
463 always co-measured, and using monthly 1-degree gridded salinity fields could introduce

464 errors. In contrast, our comparison of synthetic MOBO-DIC and the HAMOCC model
465 uses sDIC, as here we have both salinity and DIC as monthly 1-degree gridded fields.

466 4.1 Evaluation of climatological mean

467 The evaluation of the MOBO-DIC method with the synthetic data from HAMOCC
468 illustrates that the method is well-equipped to reconstruct the mean DIC fields in HAMOCC
469 well (see Table 1). MOBO-DIC reconstructs the simulated climatological mean DIC fields
470 with a negligible bias of $-1 \mu\text{mol kg}^{-1}$ and with an RMSD of $12 \mu\text{mol kg}^{-1}$.

471 The evaluation with the observational climatological constraints also reveals good
472 performance of MOBO-DIC. The mean differences relative to the Lauvset and Broullón
473 climatologies are between 7 and $10 \mu\text{mol kg}^{-1}$, and each has an RMSD of $17 \mu\text{mol kg}^{-1}$.
474 This is within the combined uncertainties of MOBO-DIC and the comparison data sets
475 (see Table 1 and Supporting Information Fig. S5 and S6). It also needs to be noted that
476 the Lauvset climatology is normalized to the year 2002, while the Broullón monthly
477 climatology is normalized to 1995. Assuming an average surface DIC increase of
478 $\sim 2 \mu\text{mol kg}^{-1}\text{yr}^{-1}$, based on the anthropogenic perturbation, we estimate that the
479 average surface concentration of MOBO-DIC (average year: 2012) is $\sim 20 \mu\text{mol kg}^{-1}$
480 higher than the surface Lauvset climatology (normalized to 2002) and $\sim 34 \mu\text{mol kg}^{-1}$
481 higher than the surface Broullón monthly climatology (normalized to 1995). The total
482 differences for the Lauvset and Broullón climatologies are less than this as the reported
483 biases in Table 1 are averages over the entire water column, but we observe surface
484 differences on these orders in Supporting Information Fig. S5 and S6.

485 Surprisingly, the bias and RMSD between the monthly climatology of MOBO-DIC
486 (Keppler et al., 2020a) and this version of MOBO-DIC is larger ($11 \mu\text{mol kg}^{-1}$ and
487 $20 \mu\text{mol kg}^{-1}$, respectively) than the RMSD between the other two climatologies that are
488 based on different methods, albeit well within the combined uncertainties. The
489 MOBO-DIC climatology is centered around the years 2010/2011, while this study is
490 centered around the year 2012. Thus, the expected surface difference should maximally be
491 of the order of $\sim 4 \mu\text{mol kg}^{-1}$. Therefore, we cannot attribute the difference to a change in
492 the periods. Instead, we found that the monthly climatology of MOBO-DIC from Keppler
493 et al. (2020a) contains less DIC in the subsurface equatorial Atlantic and Indian Ocean
494 than the Lauvset climatology (see Fig. S4 in Keppler et al. (2020a)), while our new
495 version of MOBO-DIC is more consistent with the Lauvset and Broullón climatologies (see
496 Supporting Information Fig. S5). As there are very little data in the equatorial Atlantic
497 and Indian Ocean, it is difficult to determine which of the estimates lies closer to the true
498 value. We speculate that the true value likely lies closer to the three estimates that are
499 close to each other (Lauvset, Broullón, and this study), than the one that differs (monthly
500 climatology of MOBO-DIC).

501 The biases between MOBO-DIC and the comparison data sets from time-series stations
502 and floats ranges from -5 to $16 \mu\text{mol kg}^{-1}$. As the biases are both positive and negative,
503 there is no indication of MOBO-DIC having a systematic bias towards over/underestimating
504 the global carbon content (see Table 1 and Supporting Information Fig. S9 and S10). The
505 RMSD between MOBO-DIC and these data range from $14 \mu\text{mol kg}^{-1}$ for the SOCCOM
506 floats to $42 \mu\text{mol kg}^{-1}$ for Drake Passage but are mostly between 15 and $20 \mu\text{mol kg}^{-1}$,
507 i.e., comparable to the mean global uncertainty of MOBO-DIC ($18 \mu\text{mol kg}^{-1}$). In all cases
508 except for Drake Passage, the RMSD is within the combined uncertainties of MOBO-DIC at
509 the location of the compared data set and the uncertainty of the compared data set, using
510 standard error propagation. The disagreement at Drake Passage, a well-observed time-series
511 station, is associated with large local variabilities that are not captured in MOBO-DIC and
512 are further discussed in Section 4.3.

513 Comparing MOBO-DIC at the surface with the surface DIC from OceanSODA-ETHZ,
514 we find that the magnitude and spatial patterns of the mean DIC agree very well, considering

Table 1. Summary of the bias, defined here as the mean difference (MOBO-DIC – comparison data sets), and the RMSD between MOBO-DIC and the comparison data sets. Also displayed are the mean uncertainty of MOBO-DIC at the time and location of the compared data set and the uncertainty of the comparison data sets.

Compared data set	Type of data	Bias (μ)
GLODAPv2.2021	Ship data, without interpolation or mapping (used to train the neural network)	
Lauvset climatology	Global climatology (optimal interpolation)	
Broullón climatology	Global monthly climatology (single-step neural network)	
MOBO-DIC _{clim}	Global monthly climatology (cluster-regression)	
HAMOCC	Synthetic data	
BATS	Time-series station	
HOTS	Time-series station	
Drake Passage	Time-series station (surface)	
SOCCOM floats	Calculated DIC from BGC floats (pH) with LIAR algorithm	
OceanSODA-ETHZ	Global surface estimate (cluster-regression)	

they are based on independent data (SOCAT pCO₂ vs. GLODAP DIC; Bakker et al. (2016); Lauvset et al. (2021)). The global mean RMSD between the two data sets is 15 $\mu\text{mol kg}^{-1}$, and there is a mean bias of approximately 4 $\mu\text{mol kg}^{-1}$, which is well within the uncertainties (see Table 1 and Supporting Information Fig. S11 a-c).

4.2 Evaluation of trends

Our synthetic MOBO-DIC generally reconstructs both the spatial distribution and magnitude of the trend of sDIC in HAMOCC well, with no indication of a systemic over- or underestimation of the trend (see Supporting Information Fig. S7). An exception is the deep eastern equatorial Pacific, where MOBO-DIC overestimates the trend. This could be the result of overfitting or of challenges of MOBO-DIC to fit the trends in a region with very large lateral gradients and where data coverage is intermittent. We do not see similarly large trends in the reconstructions with observations, possibly because the observed lateral gradients are smaller than those in the model. Still, this mismatch in the synthetic data suggests that the MOBO-DIC reconstructed trends are likely somewhat less robust than the climatologies and that care must be taken to avoid an overinterpretation of the results.

The sDIC trends at the time-series stations are comparable to MOBO-DIC at the times and locations of these independent observations (see Table 2 and Supporting Information Fig. S9). For example, we observe a mean trend in the water column at BATS of 7 $\mu\text{mol kg}^{-1} \text{decade}^{-1}$, while the mean trend in the water column in MOBO-DIC at the grid cell closest to BATS is $5 \pm 2 \mu\text{mol kg}^{-1} \text{decade}^{-1}$. However, some quantitative differences exist, with the largest difference in the trend found at depths between 600 and 800 m at BATS. There, MOBO-DIC, with an estimated trend of only $5 \pm 2 \mu\text{mol kg}^{-1} \text{decade}^{-1}$ underestimates the observed trend of 16 $\mu\text{mol kg}^{-1} \text{decade}^{-1}$ quite substantially. With BATS being one of the best-constrained time-series sites, the observed trend is very robust. The trend is much better reconstructed in the shallower waters at BATS, indicating that this is not a general issue but likely an issue specifically associated with the intermediate water masses in the North Atlantic.

MOBO-DIC also underestimates the trend seen in the BGC-Argo floats in the Southern Ocean (SOCCOM floats) between 20 and 40 m (see Table 2 and Supporting Information Fig. S10). The observed trend is $-20 \mu\text{mol kg}^{-1} \text{decade}^{-1}$, while the trend estimate in MOBO-DIC at the same grid cells is only $-9 \pm 2 \mu\text{mol kg}^{-1} \text{decade}^{-1}$. There is a known difference

546 between ship-based DIC measurements and DIC derived from float pH measurements (Gray
547 et al., 2018). However, this offset is thought to be relatively steady and should not affect
548 the trend. Nevertheless, the time series is short and spatially sparse, so it is not entirely
549 clear whether the issue is with MOBO-DIC or with the SOCCOM-derived DIC trend.

550 The trend of MOBO-DIC at the surface has a similar spatial distribution but is
551 slightly smaller than the trend of the mapped surface DIC from Gregor and Gruber
552 (2021), with a global mean trend between January 2004 and December 2018 of
553 $0.6 \pm 0.1 \mu\text{mol kg}^{-1} \text{ yr}^{-1}$ and $0.8 \mu\text{mol kg}^{-1} \text{ yr}^{-1}$, respectively (see Supporting Information
554 Fig. S11 d-f). As OceanSODA-ETHZ is based on considerably more surface measurements
555 than MOBO-DIC, it is likely that MOBO-DIC slightly underestimates the trend of the
556 surface DIC.

557 4.3 Evaluation of Interannual variability

558 Similar to the trend, our synthetic MOBO-DIC reconstructs the spatial distribution
559 and magnitude of the interannual variability, defined here as the standard deviation across
560 the ensemble, of sDIC in HAMOCC well (see Supporting Information Fig. S8). However,
561 we also find an artifact in the deep eastern equatorial Pacific, i.e., the same region where
562 we had difficulties with the trend. There, the interannual variability is too large in the
563 synthetic MOBO-DIC reconstruction. Again, no such artifact exists in the MOBO-DIC
564 reconstructions with observations, but smaller artifacts cannot be ruled out.

565 MOBO-DIC tends to underestimate the observed interannual variability of sDIC at the
566 time-series stations and the locations of the SOCCOM floats (see Table 2 and Supporting
567 Information Figs. S9 and S10). The biggest difference in the interannual variability is
568 between 20 and 40 m at HOT, where MOBO-DIC estimates a variability of only $4 \mu\text{mol kg}^{-1}$,
569 while the observations suggest a value of $11 \mu\text{mol kg}^{-1}$. As above, such differences can be
570 at least partially explained by the observations containing a lot of noise and not necessarily
571 being representative of the mean monthly 1° fields. At Drake Passage, the comparison data
572 displays considerably more variability than our gridded product and may include outliers.
573 Thus, there are instances where the discrepancies between MOBO-DIC and the comparison
574 data sets are beyond the uncertainty limits. We expect that this is mostly due to large local
575 variabilities that are smoothed out in the monthly mean $1^\circ \times 1^\circ$ fields in MOBO-DIC.

576 The interannual variability of MOBO-DIC at the surface also has a similar distribution
577 and is slightly smaller than the interannual variability of the mapped surface DIC from
578 Gregor and Gruber (2021) (see Table 2 and Supporting Information Fig. S11 g-i). Here, we
579 observe global mean standard deviations of 3 and $4 \mu\text{mol kg}^{-1}$, respectively (see Supporting
580 Information Fig. S11 g-i). An explanation for their slightly higher variability could lie
581 in the fact that OceanSODA-ETHZ uses satellite-based sea surface temperature (SST) as a
582 predictor while we use float data for temperature and salinity. Satellite-based SST estimates
583 are known to display more variability than float-based estimates (Roemmich & Gilson, 2009).
584 Further, OceanSODA-ETHZ has less interannual variability in pCO_2 than other surface
585 products such as SOM-FFN by Landschutzer et al. (2016). Thus, the available evidence
586 suggests that MOBO-DIC tends to underestimate the interannual variability. We suspect
587 that if time-varying monthly fields of oxygen and nutrients were available as predictors, the
588 interannual variability in MOBO-DIC might be larger. In addition, if we had more DIC
589 training data available, the interannual signal could likely be captured better.

590 5 Results and Discussion

591 5.1 Global changes in the DIC inventory

592 The reconstructed (near) global sDIC inventory between 0 and 1500 m increased steadily
593 from 2004 through 2019, with a total increase of $42 \pm 5 \text{ Pg C}$ over this period (Fig. 1). All

Table 2. Comparison of the trends (in $\mu\text{mol kg}^{-1} \text{decade}^{-1}$) and interannual variability (IAV, in $\mu\text{mol kg}^{-1}$), defined as the standard deviation in time (seasonal cycle and trend removed), from independent DIC estimates, and from MOBO-DIC at the time and locations of the independent data. Due to data sparsity in the observational data, we average the fields over depth slabs (20 to 40 m, 100 to 150 m, 600 to 800 m). The locations of the stations are illustrated in Supporting Information Fig. S1.

	Compared data set → Depth ↓	BATS	MOBO-DIC at BATS	HOT	MOBO-DIC at HOT	Drake Passage
Trend	20-40 m	1	7	5	2	
	100-150 m	3	8	13	6	
	600-800 m	16	5	4	5	
IAV	20-40 m	5	2	11	4	
	100-150 m	4	2	6	2	
	600-800 m	4	1	3	1	

depth ranges contribute to this trend, with $\sim 16\%$ of the increase in sDIC having occurred in the upper 150 m, $\sim 18\%$ between 150 and 300 m, $\sim 38\%$ between 300 and 700 m, and $\sim 28\%$ between 700 and 1500 m. Superimposed onto this strong positive trend, we observe the effect of the seasonal cycle on the total inventory (order of $\sim 2 \text{ Pg C}$), some interannual variations, and a weakening of the trend in the second half of the record, most strongly visible in the deepest depth slice analyzed, i.e., below 700 m.

By adding an estimate of the sDIC changes in the shallow coastal regions and the high latitudes ($3 \pm 0.4 \text{ Pg C}$) and in the ocean below 1500 m ($6 \pm 6 \text{ Pg C}$; see Supporting Information Section S3), we arrive at a global sDIC inventory change of $51 \pm 11 \text{ Pg C}$ over the 16 years of our analysis. This corresponds to an average rate of increase of $3.2 \pm 0.7 \text{ Pg C yr}^{-1}$. We interpret this increase in sDIC to be mostly of atmospheric origin, i.e., reflecting a net uptake of CO_2 from the atmosphere, although we cannot exclude a small contribution coming from other sources, such as a trend in the input from rivers and sediment sources, or an imbalance with the marine organic carbon pool.

Our interior ocean data-based net ocean uptake estimate of $3.2 \pm 0.7 \text{ Pg C yr}^{-1}$ is comparable with surface pCO_2 observation-based estimates of the net carbon flux from the atmosphere into the ocean. The latest update of the net air-sea CO_2 flux estimate by Landshtzer et al. (2016), which includes both the open and coastal ocean, suggests a global uptake of $2.1 \pm 0.5 \text{ Pg C yr}^{-1}$ from 2004 through 2019. Adding a riverine outgassing of CO_2 of $0.6 \pm 0.4 \text{ Pg C yr}^{-1}$ (Friedlingstein et al., 2022; Regnier et al., 2022), these surface ocean data suggest a net uptake of $2.7 \pm 0.6 \text{ Pg C yr}^{-1}$. Similar numbers are obtained when using an ensemble of surface pCO_2 data (Fay et al., 2021). This is $0.5 \pm 0.6 \text{ Pg C yr}^{-1}$ less than our estimate based on the increase in ocean interior sDIC but within the uncertainty bounds. Also, a scaled estimate of the accumulation of anthropogenic CO_2 in the ocean interior over this time period suggests a global uptake on the order of close to 3 Pg C yr^{-1} (Gruber et al., 2023). It has to be noted, as stated above, that there are still uncertainties in the surface-based estimates, due to the indirect approach that needs to incorporate the riverine flux, which has large uncertainties, and a possible skin-temperature correction (Dong et al., 2022; Watson et al., 2020). Specifically, Dong et al. (2022) suggested that the proper accounting of all temperature-related issues (e.g., skin correction) would increase the ocean uptake of the commonly used surface pCO_2 based products by $+35\%$ (0.6 Pg C yr^{-1}) for the period 1982 to 2020. If one was to use the skin correction of 0.6 Pg C yr^{-1} , as well as

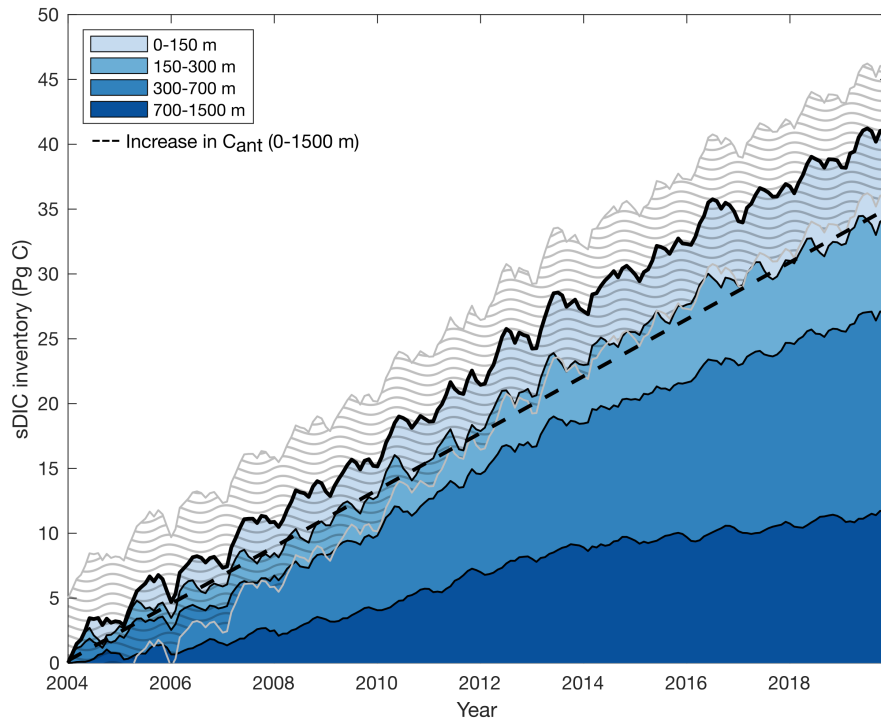


Figure 1. Temporal change in the global sDIC inventory derived from MOBO-DIC from 2004 through 2019, relative to January 2004, for different depth slabs: 0 to 150 m, 150 to 300 m, 300 m to 700 m, 700 m to 1500 m (from light blue to dark blue). The gray shading marks the uncertainty around the upper 1500 m. The dashed black line illustrates the estimated increase in C_{ant} based on ΔC_{ant} from 1800 to 2007 scaled to the same period, using a scaling factor α of 0.29.

626 the 0.6 Pg C yr^{-1} riverine flux, this would yield a total flux of $3.3 \pm 0.6 \text{ Pg C yr}^{-1}$, which is
 627 remarkably close to our estimate of $3.2 \pm 0.7 \text{ Pg C yr}^{-1}$.

628 Our estimate of the total increase in ocean sDIC of $51 \pm 11 \text{ Pg C}$ implies that from
 629 2004 through 2019, the ocean sink accounted for $\sim 31 \pm 7\%$ of the total anthropogenic CO_2
 630 emissions (here: from fossil fuel emissions and land-use change, Friedlingstein et al. (2022)).
 631 This uptake fraction is larger but within the uncertainties compared to the fraction reported
 632 by the Global Carbon Project based on ocean models and surface ocean pCO_2 products
 633 during the decade 2011 to 2020 ($26 \pm 4\%$, Friedlingstein et al. (2022)). As pointed out by
 634 Friedlingstein et al. (2022), within the Global Carbon Budget estimates, it is particularly
 635 the hindcast model-based estimates that indicate a smaller uptake. Similarly, Terhaar et
 636 al. (2022) used an emergent constraint approach to demonstrate that most CMIP models
 637 tend to take up too little CO_2 from the atmosphere. Although CMIP models differ from
 638 the hind-cast models used in the Global Carbon Budget, these findings further indicate
 639 that the models underestimate the oceanic carbon uptake, as also discussed by Hauck et
 640 al. (2020). Our interior ocean-based estimate thus supports the larger (mostly observation-
 641 based) estimates of the ocean carbon sink in the Global Carbon Budget, albeit within large
 642 uncertainties.

643 Another reference point is the oceanic accumulation of C_{ant} between 2004 and 2020.
 644 Lacking an estimate of the C_{ant} accumulation over the same period, we scale the estimates

of Sabine et al. (2004) and Gruber et al. (2019) to this period, assuming a transient steady-state (see Section 2.4). We obtain a global increase of 44 ± 6 Pg C (2.8 ± 0.4 Pg C yr⁻¹) in C_{ant} (1800-2007 scaled to 2004-2019 with a scaling factor of 0.29) and 49 ± 6 Pg C (3.1 ± 0.4 Pg C yr⁻¹) in C_{ant} (1994-2007, scaled to 2004-2019 with a scaling factor of 1.45). The estimates are remarkably close to our estimate of the increase in total sDIC (51 ± 11 Pg C, i.e., 3.2 ± 0.7 Pg C yr⁻¹). This suggests that we can largely attribute the reconstructed increase in the sDIC to the uptake of anthropogenic CO₂ from the atmosphere. Similarly, when only considering the domain of MOBO-DIC and without upscaling, we also find that the trend in MOBO-DIC (40 ± 5 Pg C, i.e., 2.5 ± 0.3 Pg C yr⁻¹) is close to the increase in C_{ant} over the same period and domain (35 ± 4 Pg C, i.e., 2.2 ± 0.2 Pg C yr⁻¹, dashed line in Fig. 1), and also well within the uncertainties. Considering the proposed outgassing signal of C_{nat} (McNeil & Matear, 2013), this would have been reflected in a weaker trend in total sDIC than in C_{ant} ; however, we do not observe this during our study period. This finding is in-line with the recent review by Gruber et al. (2023) who also concluded that the trend in the oceanic carbon sink was primarily driven by the increasing uptake of C_{ant} and that the proposed loss of C_{nat} can at this stage not be conclusively quantified with observations.

Superimposed onto this positive long-term trend of sDIC, the reconstructions reveal substantial interannual variations and a weakening of the trend after ~ 2012 , especially in the deeper waters. The following sections will further discuss these variations and the weakening trend. We also dive deeper into the differences between the anthropogenic component and the total sDIC in the water column, revealing changes in the natural DIC pool. Additionally, we find a strong seasonal signal, most pronounced near the surface. We do not discuss the seasonal variations near the surface, as the seasonal cycle of DIC was explored in Kepler et al. (2020b).

5.2 Regional distribution of trends in sDIC, C_{ant} , and C_{nat}

The rate of the depth-integrated accumulation of sDIC is regionally strongly structured (Fig. 2a), with the highest rates of accumulation found in the North Atlantic south of Iceland, i.e., the Subpolar Gyre. There, the linear trend exceeds 1.5 mol m⁻² yr⁻¹. An additional region with elevated rates of increase can be identified in the southern hemisphere between about 20°S and 45°S with typical accumulation rates of ~ 1 mol m⁻² yr⁻¹. The higher latitudes of the Southern Ocean, the tropical regions, the northern Indian, and particularly the North Pacific have considerably weaker depth-integrated changes in sDIC, typically 0.5 mol m⁻² yr⁻¹ or less. In some regions of the North Pacific, the depth-integrated sDIC even decreases over our study period. This vertical integral is a robust feature of our analysis as it is only weakly changing when removing trends within the water column that are not significant (compare Supporting Information Fig. S12 with Fig. 2a).

At each depth level, most of the trends in sDIC are statistically significant (95% confidence interval, see Supporting Information Section S7 and Fig. S12). This is also the case for the negative trends in the North Pacific. Further support comes from the existence of a comparable negative trend in the surface DIC reconstructions of the OceanSODA-ETHZ product (Gregor & Gruber, 2021), as demonstrated in Section 4.2 and Supporting Information Fig. S11. Thus, this negative signal in the North Pacific appears robust within our period and is not an artifact of our method.

Next, we examine the similarity between the rate of depth-integrated accumulation of sDIC and C_{ant} , which becomes even more evident when they are put side by side, irrespective of how we estimated the expected change in C_{ant} from 2004 through 2019. The patterns and magnitude of the depth-integrated accumulation of sDIC (Fig. 2a) and the two different estimates of C_{ant} (Fig. 2b,c) are to the first order approximately the same, as also evidenced by their high pattern correlation coefficient $c = 0.56$ and 0.63 , between the trend in MOBO-

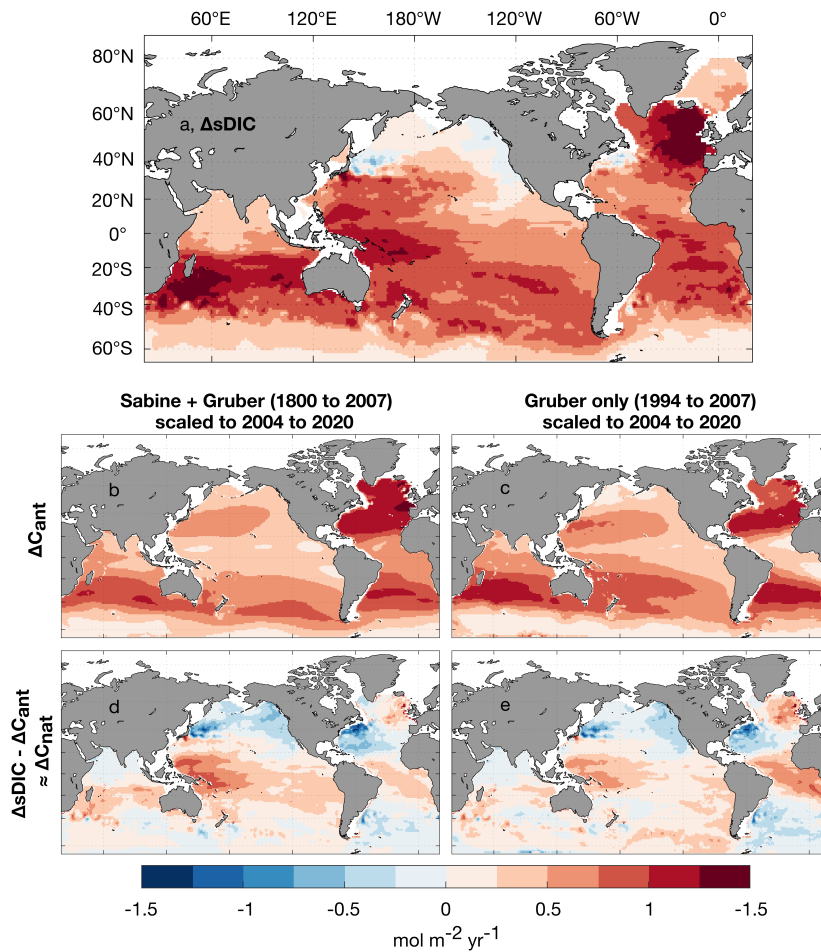


Figure 2. Maps of the column-integrated (upper 1500 m) (a) change in sDIC from 2004 through 2019 based on the linear trend, (b,c) change in C_{ant} scaled to the same period (2004 through 2019), and (d,e) the anomalous change (i.e., approximately the change in C_{nat}) from 2004 through 2019, estimated from the difference between the change in the MOBO-DIC inventory [illustrated in (a)], and the change in the C_{ant} inventory, scaled to the same period as (a) [illustrated in (b) and (c)]. For the combined estimate of C_{ant} by Sabine et al. (2004) (1800 to 1994) and Gruber et al. (2009) (1994 to 2007) (b,d) and for the estimate of C_{ant} by Gruber et al. (2009) (1994 to 2007; c,e). Scaling on the basis of the transient steady-state model ($anom = \Delta MOBO-DIC - \alpha \cdot \Delta C_{ant}$, $\alpha = 0.29$ for the period 1800-2007 and $\alpha = 1.45$ for the period 1994-2007). See Supporting Information Fig. S12 for the trends in MOBO-DIC on individual depth levels.

696 DIC and the scaled ΔC_{ant} from the combined estimate by Sabine et al. (2004) and Gruber et
 697 al. (2019), and the estimate by Gruber et al. (2019), respectively. For example, we observe in
 698 all fields a large increase in the North Atlantic and a broad band of enhanced accumulation
 699 in the mid-latitudes of the Southern hemisphere. Also present in all fields is the weaker
 700 signal in the mid-latitude Southern Ocean. This further supports the conclusion that most
 701 of the column-integrated change in sDIC can be attributed to the increase in C_{ant} during
 702 this period.

703 However, there are also several notable differences, discernible when we subtract the
704 estimated anthropogenic component (i.e., ΔC_{ant}) from the reconstructed change in sDIC
705 (Fig. 2d,e). This difference can be interpreted as the change in the natural oceanic CO₂
706 component of DIC, i.e., ΔC_{nat} , although given our steady-state assumption when estimating
707 ΔC_{ant} , this difference can also contain an element of the non-steady-state, i.e., climate
708 variability induced, component of ΔC_{ant} . The North Pacific stands out as the region with
709 the biggest loss in C_{nat} . In addition, C_{nat} is lost in the upwelling region of the Atlantic
710 sector of the Southern Ocean and the Subtropical Gyre of the North Atlantic. These losses
711 of C_{nat} are counter-balanced by gains of C_{nat} in the tropics and the Indo-Pacific sector
712 of the Southern Ocean. Furthermore, in the North Atlantic Subpolar Gyre, a region of
713 strong uptake of C_{ant} , we also observe an increase in C_{nat} . Integrating ΔC_{nat} yields a total
714 increase of $0.4 \pm 0.8 \text{ Pg C yr}^{-1}$, and $0.1 \pm 0.8 \text{ Pg C yr}^{-1}$, for C_{nat} based on the combined
715 estimate (Sabine et al., 2004; Gruber et al., 2019), and the estimate by Gruber et al. (2019),
716 respectively. Given the lack of statistical significance, we conclude that we cannot detect a
717 global change in C_{nat} during our study period.

718 Nonetheless, the reduction of ΔC_{nat} in the North Pacific stands out. We link this
719 change to the phasing of the Pacific Decadal Oscillation (PDO) as it shifted between 2004
720 and 2019 from positive to negative. While negative PDO regimes are associated with a
721 shallow thermocline in the Kuroshio Extension, which results in deep mixing and cooler
722 SSTs in the North Pacific, positive PDO regimes are associated with warmer SSTs (Mantua
723 & Hare, 2002). Thus, we speculate that during our analysis period, the shoaling of the
724 thermocline in the North Pacific brought DIC stored at depth to the surface, allowing it to
725 outgas, leading to an overall loss of DIC in this region. We expect that the opposite would
726 occur during positive phases of the PDO so that the net change over multiple decades
727 would be close to zero, and thus not impact the long-term trend. To test this hypothesis,
728 we plotted the trend in the surface sDIC from OceanSODA-ETHZ (Gregor & Gruber, 2021)
729 over their entire study period (1985 through 2018). Over that extended period, we do not
730 observe negative trends in surface sDIC in the North Pacific (not shown), indicating that
731 the observed negative trend in the North Pacific sDIC and C_{nat} between 2004 and 2019 is
732 not a long-term signal. The loss of C_{nat} in the North Pacific during our analysis period
733 is partially balanced by a gain in C_{nat} in most parts of the Indo-Pacific, especially in the
734 Western tropical Pacific. We find that this signal is associated with the phasing of the
735 El Niño Southern Oscillation (ENSO), as further discussed in Supporting Information Fig.
736 S13. We speculate that over a longer period than our 16 years, this signal of increased C_{nat}
737 in the Western tropical Pacific would also be dampened.

738 Similarly, we link the changes in C_{nat} in the North Atlantic to the phasing of the
739 Atlantic Multidecadal Oscillation (AMO; Kerr (2000) as between 2004 and 2019, the AMO
740 index moved from positive to negative (see [https://climatedataguide.ucar.edu/
741 climate-data/atlantic-multi-decadal-oscillation-amo](https://climatedataguide.ucar.edu/climate-data/atlantic-multi-decadal-oscillation-amo)). Negative AMO phases are
742 associated with increased vertical mixing in the North Atlantic Subpolar Gyre, and thus,
743 an increase of upper ocean DIC and C_{nat} in this region (Breedon & McKinley, 2016).
744 Concurrently, in the North Atlantic Subtropical Gyre, negative AMO phases are
745 associated with a decrease in DIC and C_{nat} in this region due to changes in the
746 temperature affecting the solubility of CO₂. In the tropical Atlantic, the increase in C_{nat}
747 during our study period might be associated with teleconnections from the AMO phasing.
748 The loss of C_{nat} in the South Atlantic is in line with the findings by Keppeler and
749 Landshtzer (2019) who reported a weakening of the Southern Ocean carbon sink in the
750 Atlantic sector since ~ 2012 . They linked this weakening to shifts in sea level pressure and
751 associated changes in surface winds. We note that these links between changes in C_{nat} and
752 the PDO and the AMO are speculative at this point, as the relatively short temporal
753 extent of MOBO-DIC (16 years) prevents us from robustly concluding on the effect of
754 multi-decadal modes of variability.

755 Fig. 3 reveals how the trend in sDIC varies with depth at the scale of entire ocean
 756 basins split into latitude bands (black line). Near the surface, sDIC is reconstructed to
 757 have increased, on average by about $0.6 \mu\text{mol kg}^{-1} \text{yr}^{-1}$, with some regions having a higher
 758 accumulation (e.g., $0.8 \mu\text{mol kg}^{-1} \text{yr}^{-1}$ in the North Atlantic) and other regions less (e.g.,
 759 $0.3 \mu\text{mol kg}^{-1} \text{yr}^{-1}$ in the North Pacific). In all regions, the trend in sDIC increases
 760 between the mixed layer and the intermediate waters and then decreases with depth below
 761 that, reaching values of around $0.2 \mu\text{mol kg}^{-1} \text{yr}^{-1}$ at 1500 m. We observe the largest
 762 increase in sDIC in the Atlantic between ~ 200 m and 500 m ($\sim 0.9 \mu\text{mol kg}^{-1} \text{yr}^{-1}$).

763 Comparing the temporal trends in sDIC with the estimated changes in C_{ant} (blue
 764 and red lines in Fig. 3) highlights strong similarities but also distinct differences. Near the
 765 surface, sDIC increased less than C_{ant} during our study period. This difference is significant
 766 in all regions except for the Southern Ocean and North Atlantic. In the deeper ocean, the
 767 difference between the trend in sDIC and ΔC_{ant} is not significant in the Southern Ocean,
 768 North Pacific, tropical Indian Ocean, and the South Atlantic, while in the other regions, the
 769 trend in sDIC tends to be larger than the two estimates of ΔC_{ant} . The differences between
 770 the trends in sDIC compared to those in C_{ant} imply a loss of C_{nat} in the upper ocean and a
 771 gain of C_{nat} in the ocean's interior below a few hundred meters depth. Combined with the
 772 lack of an overall change in C_{ant} , this suggests a strong internal redistribution of oceanic
 773 C_{nat} over our analysis period.

774 We tested the robustness of our inferred ocean internal redistribution of C_{nat} by
 775 comparing them to data from repeat hydrographic lines obtained as part of the Global
 776 Ocean Ship-based Hydrographic Program (GO-SHIP; Talley et al. (2016)). In Supporting
 777 Information Figure S14, we compare the change in DIC between different occupations of
 778 the same line with the reconstructed change in MOBO-DIC at the same locations over the
 779 same period, and also with the changes in C_{ant} scaled to the same period. We find that
 780 the change in DIC (both at the repeated GO-SHIP tracks and in MOBO-DIC) differs
 781 substantially from the ΔC_{ant} profiles, in a similar way as demonstrated when we average
 782 over large regions in Fig. 3. This adds a second line of evidence that the vertical
 783 redistributions of C_{nat} that we discuss here are not artifacts from our method but are also
 784 directly visible in the ship measurements from the GO-SHIP program. We note that the
 785 magnitude of the trend in DIC is larger when only considering the grid cells of the
 786 GO-SHIP tracks (Supporting Information Fig. S14), than when averaging over large
 787 regions (Fig. 3), due to a tendency for opposing trends canceling each other when the
 788 profiles are averaged over large regions.

789 The similarities and differences in the vertical distribution of the trends in sDIC, C_{ant} ,
 790 and C_{nat} become even more evident when analyzing zonal mean sections of these components
 791 (Fig. 4). Due to methodological constraints, there are some discontinuities at 500 m in the
 792 MOBO-DIC derived sDIC (Fig. 4a-c), which are associated with boundaries generated by
 793 the depth slabs. Aside from that, the trend in sDIC and ΔC_{ant} (Fig. 4d-f) are very similar,
 794 as noted above for the mean profiles. This figure again highlights the loss of C_{nat} (Fig.
 795 4g-i) at the surface, except in the North Atlantic. We also observe a loss of C_{nat} in the
 796 North Pacific, extending down to 1500 m but most pronounced in the upper ~ 800 m. The
 797 northern high latitudes tend to lose C_{nat} at depth, while the low latitudes tend to gain C_{nat}
 798 at depth. Overall, the redistribution of C_{nat} occurs both horizontally, as demonstrated in
 799 Fig. 2, and vertically (Fig. 3 and 4), but as pointed out above, the signal in C_{nat} is within
 800 the uncertainty bounds.

801 We cannot identify the potential reasons for this redistribution, but the upper ocean
 802 loss of C_{nat} may be at least partially driven by the warming of the ocean, which is strongest
 803 in the upper ocean (IPCC, 2021). In addition, such a redistribution pattern is reminiscent
 804 of the impact of the ocean's biological pump, where an increased efficiency of this pump
 805 would lead to a depletion of C_{nat} in the upper ocean and an accumulation at depth. As
 806 we observe this pattern most prominently in the tropics, we speculate that biology may be
 807 driving the change in sDIC here. Conversely, as we already hypothesized above, the other

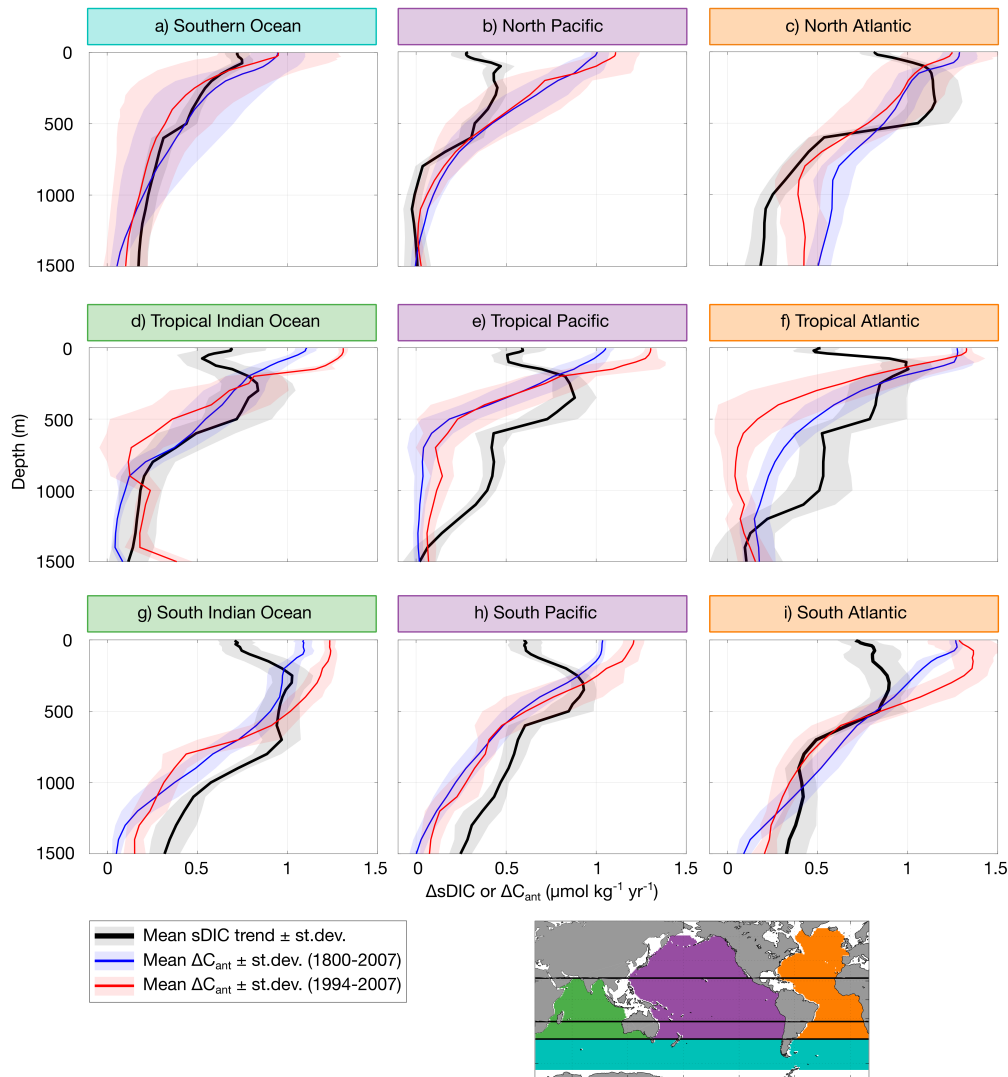


Figure 3. Vertical profiles of the mean trend in subregions for sDIC estimated by MOBO-DIC (black) and ΔC_{ant} from 1800 to 2007 scaled to the period 2004 through 2019 (blue), and from 1994 to 2007, scaled to 2004 through 2019 (red). The uncertainty of the trend in sDIC, based on the standard deviation across the trend in the 15 ensemble members, is illustrated in shading. The uncertainty of the trend in ΔC_{ant} , based on the standard deviation in the latitude-longitude space, is illustrated in shading. Separately for the Southern Ocean (a), Indian Ocean (d,g), Pacific (b,e,h), Atlantic (c,f,i), in the northern temperate regions (until 23°N , b,c), the tropics (23°N to 23°S , d-f), and in the southern temperate regions (from 23°S to 40°S , g-i). The map at the bottom indicates the limits of the ocean basins in color, and the climatic regions are delimited by black lines.

808 regions, including the North Pacific, North Atlantic, and Southern Ocean are likely driven
809 by physical changes.

810 It should also be noted that the vertical profile in the trend is strongly influenced by
811 interannual variations, such as variations in the thermocline and surface outgassing. Thus,
812 the signal in the mixed layer is prone to large interannual to decadal variations, which are

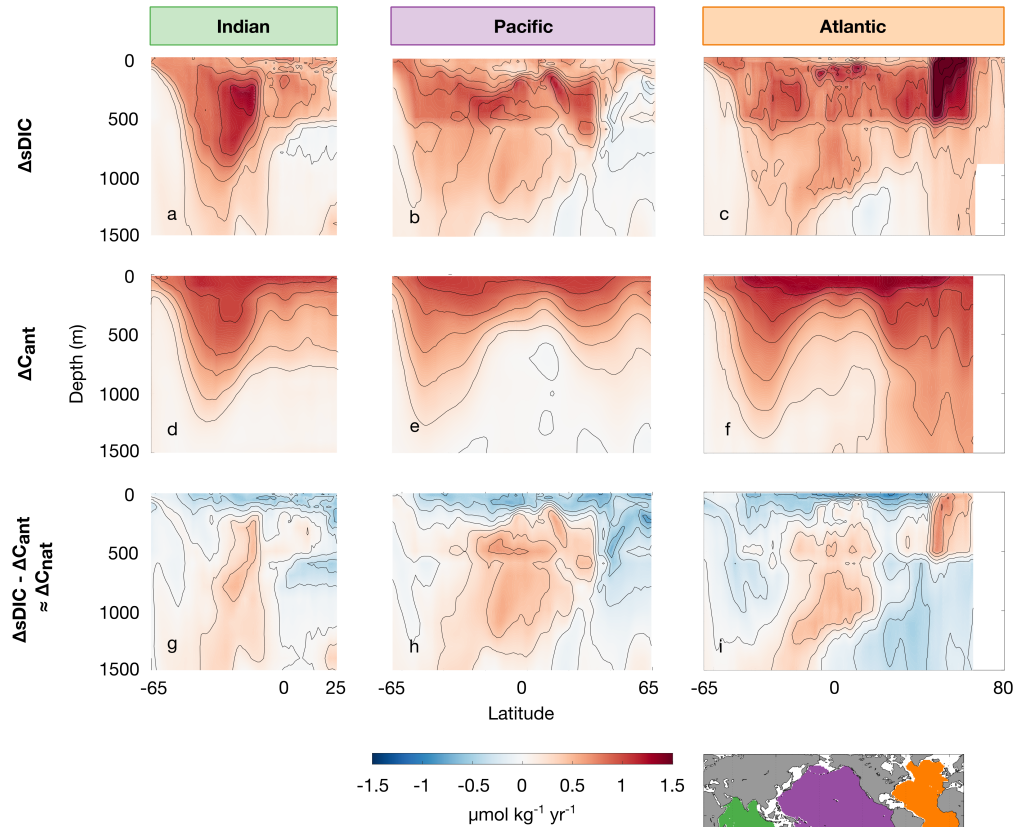


Figure 4. Zonal mean sections of the trend in sDIC from 2004 through 2019 (a-c), of ΔC_{ant} from 1800 to 2007, scaled to our period (d-f), and the difference between the two, i.e., ΔC_{nat} (g-i), for the Indian Ocean (a,d,g), Pacific (b,e,h), and the Atlantic (c,f,i). The map at the bottom right illustrates the boundaries of the basins.

especially dominant in the Southern Ocean (Le Qur et al., 2007; Landschutzer et al., 2015; Keppler & Landschutzer, 2019). Therefore, the observed trends in the mixed layer depend greatly on the start and end year and should be interpreted with care. A longer time series would yield a result more representative of the anthropogenically forced trend.

5.3 Interannual variability at global and basin-scale

The interannual variability of sDIC, defined here as the standard deviation in time (seasonal cycle and trend removed), is rather small in our product, especially when compared to the magnitude of the trend (previous section) and the amplitude of the seasonal cycle (Keppler et al., 2020b). With a global mean temporal standard deviation of $2 \mu\text{mol kg}^{-1}$ at 150 m (the depth level with the largest mean standard deviation), compared to a global mean uncertainty of $18 \mu\text{mol kg}^{-1}$ at 150 m, the interannual variability is well within the product uncertainty of MOBO-DIC in most parts of the ocean. However, as highlighted in Section 4.3, MOBO-DIC likely underestimates the interannual variability.

Nevertheless, some clear regional signals of the interannual variability emerge (Fig. 5): the largest interannual signal is generally in the thermocline region (~ 150 m), while in the

828 mixed layer and below 700 m, the interannual variability is minimal. The equatorial Pacific
 829 stands out as a region with the largest variance, while we observe very little interannual
 830 variability in the Southern Ocean, a region with large decadal variability in the air-sea CO₂
 831 flux estimates (Le Qur et al., 2007; Landshtzer et al., 2015; Keppler & Landshtzer, 2019).
 832 A recent study has suggested that the decadal variations of the air-sea CO₂ fluxes in the
 833 Southern Ocean may be overestimated in the mapped surface estimates (Gloege et al., 2021);
 834 however, the strongest variations occur around the year 2000 (see, e.g., Friedlingstein et al.
 835 (2022)), i.e., before the start of our time-series here.

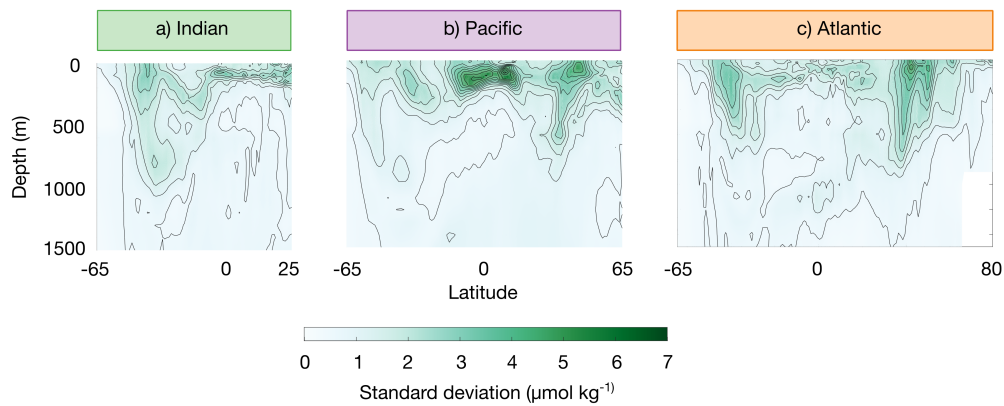


Figure 5. Zonal mean sections of the interannual variability of sDIC, defined as the standard deviation of the time-dimension of sDIC (detrended, seasonal cycle smoothed with a 12-month running mean) for the Indian (a), Pacific (b), and Atlantic Oceans (c). See the map at the bottom right of Fig. 4 for the boundaries of the basins.

836 We further illustrate the nature of the mean vacillations of the vertically integrated sDIC
 837 (upper 1500 m) for large subregions in Fig. 6. The most dominant interannual variations
 838 are found in the Pacific, where we see a steep increase in sDIC between 2010 and 2014 in the
 839 tropics. The northern temperate Pacific also stands out: Here, the trend in sDIC is initially
 840 weak until 2010, increases until 2014, and then we observe a negative trend until the end of
 841 the time series in December 2019. Both in the northern and southern temperate regions of
 842 the Atlantic, the sDIC trend has weakened since around 2012. In contrast, averaged over the
 843 whole Southern Ocean, we find very few interannual variations here. Similarly, the Indian
 844 Ocean, the South Pacific, and the tropical Atlantic all vary little interannually in the upper
 845 1500 m when averaging over these areas.

846 We link the sDIC increase in the tropical Pacific at least partially to a shift from La
 847 Niñas (especially in 2008 and 2011) to El Niños (especially in 2015 and 2019, see
 848 Supporting Information Fig. S13). The other ENSO-related signals during our study
 849 period are considerably weaker and seem mostly dampened when considering the whole
 850 tropical Pacific. The large variation in the North Pacific is likely to be influenced by the
 851 phasing of the PDO, but may also have an ENSO-related teleconnection. We find that the
 852 weakening of the vertically integrated sDIC around 2012, illustrated in Fig. 1, stems
 853 largely from the high latitude South Atlantic and the tropical Pacific. The weakening of
 854 the sink in the high latitude South Atlantic is in line with the findings by Keppler and
 855 Landshtzer (2019), who report a weakening of the CO₂ uptake in the Atlantic sector of
 856 the Southern Ocean around 2012. While this signal is not dominant when averaging over
 857 the whole Southern Ocean, this weakening sink around 2012 is also visible in the global
 858 changes in sDIC (Fig. 1), highlighting the important role of the Southern Ocean carbon
 859 uptake (here: specifically its Atlantic sector) globally. A longer time series is needed to

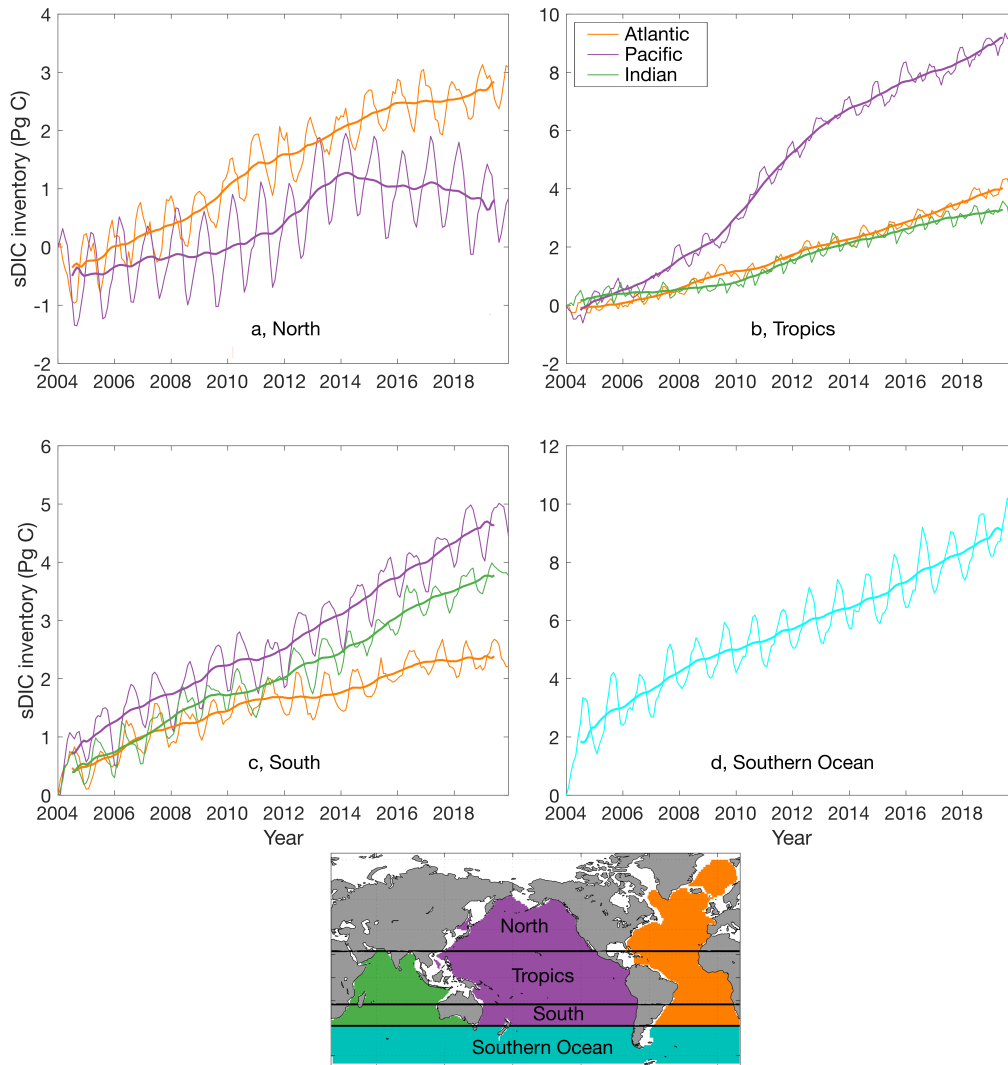


Figure 6. Timeline of the vertical integral (upper 1500 m) of sDIC relative to January 2004 (think solid lines) in the northern temperate regions (a), tropics (b), southern temperate regions (c), and the Southern Ocean. In a-c, separately for the Atlantic (orange), Pacific (purple), and Indian Ocean (green). Note that the y-axes differ in each subplot. Thick solid lines have the seasonal cycle smoothed with a 12-month moving average (first and last six months removed). The inserted map illustrates the boundaries of the subregions.

860 investigate if this is a long-term decline or part of multi-decadal oscillations, such as the
 861 AMO. We know from previous studies that this weakening may be due to changes in the
 862 circulation, as suggested by DeVries et al. (2017) or linked to atmospheric circulation, as
 863 proposed by Keppler and Landschutzer (2019). An alternative hypothesis for these changes
 864 is that volcanoes are the driving force for such sudden changes (McKinley et al., 2020).
 865 However, during our study period, no large volcanic eruptions occurred that may explain
 866 the observed signals.

6 Caveats and Uncertainties

Given the sparsity of DIC observations, our product fills substantial observational gaps in time and space. However, our evaluation with independent data provides confidence in the robustness of the presented numbers within the uncertainty limits. Nonetheless, there are good reasons to conclude that MOBO-DIC tends to underestimate the trend and interannual variability. Although this underestimation is within the uncertainty limits, it could be significant when integrating in the water column (see Main Text Section 4 and Supporting Information Sections S5 and S6). Further research should be conducted on this, especially as more data becomes available with future GLODAP releases and BGC Argo data.

The uncertainties of the MOBO-DIC estimated sDIC at the level of a single grid cell are relatively large (global mean of $18 \mu\text{mol kg}^{-1}$) and are often larger than the signal in the trend or variability. As our mapping method minimizes the overall bias between the target data (i.e., the GLODAP DIC measurements) and the mapped estimate, we can assume that any local imprecisions average out when integrating or averaging over large areas. This means that MOBO-DIC is most robust when considering large areas, while analyses at single grid cells should be interpreted carefully, keeping in mind the uncertainty bounds. In this study, we present such integrals and averages over whole ocean basins.

We want to note that the linear trend analysis used to quantify and assess the long-term changes in DIC has its limitations, too. First, it is not a given that the increase in oceanic carbon is, in fact, linear. Second, the linear trends are based on a relatively short period of 16 years, and thus, the conditions of the start and end years tend to considerably affect the trend over such a short period (Fay & McKinley, 2013). Furthermore, decadal variations might also affect the linear trends. We found that, locally, some trends are not robust (see Supporting Information Fig. S12) but anticipate that our global trend estimate is robust within the uncertainty, as overestimates of the trend in some regions are likely to be balanced by underestimates elsewhere.

Our comparison with C_{ant} also relies on many assumptions. First, as there is not yet a published estimate of C_{ant} for the current period, we scaled previous estimates to our period, assuming a steady state (see Section 2.4). Further, our estimate of C_{nat} is based on the difference in the change in total sDIC and ΔC_{ant} . However, due to the steady-state assumption when estimating ΔC_{ant} , the difference may also contain an element of the non-steady-state component of anthropogenic ΔC_{ant} . Thus, the analyses with C_{ant} and C_{nat} could be improved in the future by using a C_{ant} estimate of the same period.

7 Summary and Conclusions

This release of the Mapped Observation-Based Oceanic Dissolved Inorganic Carbon (MOBO-DIC) extends the climatological estimate by Keppler et al. (2020b) in time, thus giving insights into the spatiotemporal evolution of the ocean DIC stock at a monthly resolution from January 2004 through December 2019. With a spatial resolution of 1° , extending from 65°N to 65°S , and until 80°N in the Atlantic, and covering the entire upper and middle ocean (depths from 2.5 m to 1500 m on 28 uneven depth levels) this dataset provides a near-global view. We conducted an in-depth validation of our new data product, which considers sources of uncertainties from the measurements, representation errors, and uncertainties stemming from our mapping method. We trust that our estimate of DIC is robust within the uncertainty ranges provided (global mean uncertainty at the individual grid cell level of $18 \mu\text{mol kg}^{-1}$).

Our analysis of the trend in sDIC provides the first direct assessment of the changes in the total sDIC stock (natural + anthropogenic) based on observations. It should be noted that at large scales, the changes in sDIC and DIC are numerically equal because the trend in salinity is negligible once integrated vertically and over large regions (Cheng et al., 2020).

Our estimate of the global increase of sDIC during our study period (3.2 ± 0.7 Pg C yr⁻¹) is approximately $31 \pm 7\%$ of the anthropogenic CO₂ emissions from fossil fuels and land use change during our study period (Friedlingstein et al., 2022). We find that this increase in sDIC is largely associated with the increase in anthropogenic carbon (C_{ant}) during this period (2.8 ± 0.4 Pg C yr⁻¹ or 3.1 ± 0.4 Pg C yr⁻¹, depending on the method).

MOBO-DIC also allows for the first assessment of changes in natural oceanic carbon (ΔC_{nat}) by subtracting ΔC_{ant} from the changes in the total sDIC, yielding a statistically insignificant global mean ΔC_{nat} of 0.4 ± 0.8 Pg C yr⁻¹ or 0.1 ± 0.8 Pg C yr⁻¹, depending on the method used to estimate C_{ant} . Previous studies had suggested a potential outgassing of C_{nat} due to elevated sea surface temperatures (McNeil & Matear, 2013), which would affect the global climate. While the large uncertainties in MOBO-DIC and C_{ant} do not rule out such a net outgassing signal of C_{nat} , we observe no statistically detectable change in C_{nat} between 2004 and 2020, in-line with the recent review by (Gruber et al., 2023). Instead, our analysis reveals a redistribution of C_{nat} - a phenomenon that had not been previously investigated at a global scale. During our study period, the upper ocean appears to have mostly lost C_{nat} , while below that, large parts of the ocean increased in C_{nat} . The loss of C_{nat} near the surface could be driven by increased ocean temperatures, as proposed by IPCC (2021). The redistributions in the Pacific correspond to the phasing of ENSO and the PDO, while the redistributions in the North Atlantic correspond to the phasing of the Multidecadal AMO. However, at this stage, our study period from 2004 through 2019 is too short to robustly conclude on (multi-) decadal signals.

The interannual variability in sDIC is substantially weaker than the seasonal cycle and temporal trend in most parts of the ocean. However, it should be noted that MOBO-DIC likely underestimates the interannual variability. We find a mean standard deviation in time of detrended, deseasonalized sDIC at the depth level with the largest variability (150 m) of $2 \mu\text{mol kg}^{-1}$. Our results demonstrate that most of the global-scale variations in sDIC stem from the North and tropical Pacific, in correspondence with ENSO and the PDO, and to a lesser extent from the high latitude South Atlantic. We further find a weakening of the positive trend in the high-latitude South Atlantic around the year 2012. This signal is also visible in the global integral of sDIC, and future studies should examine the continued evolution of this signal as well as its drivers. The interannual variations are comparably weak in the other sectors of the Southern Ocean and the Indian Ocean.

We can now constrain the ocean carbon sink from surface measurements in combination with riverine flux estimates (previous studies) and based on the direct DIC measurements that reflect the changes in the DIC pool at timescales from sub-annual to inter-annual (this study). While the surface-based estimates benefit from more observations, large uncertainties are associated with such an indirect approach. The interior perspective suffers from considerably less data but, due to the direct approach, does not need a riverine flux adjustment or gas transfer parametrization. The two perspectives each have their strengths and weaknesses, so having both perspectives substantially improves our understanding and the quantification of the global ocean carbon sink. The two estimates are in good agreement (3.2 ± 0.7 Pg C yr⁻¹ and 2.7 ± 0.6 Pg C yr⁻¹ for the interior and surface perspective, respectively), despite being based on independent data (SOCAT vs. GLODAP). However, the surface-based estimates would be larger (i.e., closer to our estimate) when considering a larger riverine flux estimate (e.g., 0.8 ± 0.4 Pg C yr⁻¹ by Resplandy et al. (2018), compared to 0.6 ± 0.4 Pg C yr⁻¹ by Friedlingstein et al. (2022) used in this study). In addition, the agreement between the surface-based estimates and our interior ocean estimate would be even higher if the proposed temperature corrections were applied to the surface estimates. Specifically, Dong et al. (2022) estimated that accounting for these corrections would increase the ocean uptake of the surface pCO₂ based products by 0.6 Pg C yr⁻¹ from 1982 through 2020.

Further, within the Global Carbon Budget (Friedlingstein et al., 2022), the observation-based methods that estimate the carbon fluxes based on surface measurements are higher

970 than the model-based estimates. Our analysis from the interior ocean perspective suggests
971 that the true value likely lies closer to the observation-based surface estimates in the Global
972 Carbon Budget than to the model-based estimates, as also suggested by Terhaar et al.
973 (2022). Thus, the current approach of averaging all ocean carbon sink estimates from
974 observations and models in the Global Carbon Budget could be revisited and improved to
975 obtain the best estimate, e.g., by weighting the observation-based estimates stronger than
976 the models.

977 Our new data product is available for the scientific community and can be used to
978 further investigate the temporal changes in DIC and its effect on marine organisms.
979 Potential further insights into the processes and drivers could be gained by prolonging the
980 timespan and investigating the multi-decadal variations. Additionally, our product
981 provides the basis to compare the decadal variations of observation-based DIC to the
982 changes in the upper Meridional Overturning Circulation, which weakened in the 1980s,
983 strengthened in the 1990s, and weakened again in the 2000s (DeVries et al., 2017).
984 Similarly, further comparing the decadal variations of the Southern Ocean carbon sink
985 (Le Qur et al., 2007; Landschutzer et al., 2015; Keppler & Landschutzer, 2019) to the
986 variations in the DIC pool in this region could lead to important new insights on the
987 global carbon cycle.

988 Acknowledgments

989 The research leading to these results has received funding from the European
990 Community's Horizon 2020 Project under grant agreement no. 821003 (4C). This work
991 was also sponsored by NSF's Southern Ocean Carbon and Climate Observations and
992 Modeling (SOCCOM) Project under the NSF Awards PLR-1425989 and OPP-1936222,
993 with additional support from NOAA and NASA. The authors are grateful for the Argo
994 data collected and made freely available by the International Argo Program and the
995 national programs that contribute to it (<https://www.argo.ucsd.edu> and
996 <https://argo.jcommops.org>). The Argo Program is part of the Global Ocean Observing
997 System. This publication uses Hawaii Ocean Time-series observations supported by the
998 U.S. National Science Foundation under Grant OCE-1260164. It also used data from the
999 Southern Ocean Carbon and Climate Observations and Modeling project (SOCCOM).
1000 Data were collected and made freely available by SOCCOM, funded by the National
1001 Science Foundation, Division of Polar Programs (NSF PLR-1425989), supplemented by
1002 NASA and by the International Argo Program and the NOAA programs that contribute
1003 to it. This work benefited from discussions with Birgit Klein (BSH), Jochem Marotzke
1004 (MPI-M), Johanna Baehr (UHH), and Jens D. Müller (ETHZ).

1006 Data availability

1007 The MOBO-DIC data product created during this study is freely available from
1008 NCEI/OCADS:
1009 <https://www.ncei.noaa.gov/data/oceans/ncei/ocads/metadata/0277099.html> and
1010 should be cited as Keppler, Lydia; Landschützer, Peter; Lauvset, Siv K.; Gruber, Nicolas
1011 (2023). Mapped Observation-Based Oceanic Dissolved Inorganic Carbon Monthly fields
1012 from 2004 through 2019 (MOBO-DIC2004-2019) (NCEI Accession 0277099). [indicate
1013 subset used]. NOAA National Centers for Environmental Information. Dataset.
1014 <https://doi.org/10.25921/z31n-3m26>. Accessed [date].

1015 The GLODAP DIC ship measurements are available at
1016 <https://www.ncei.noaa.gov/data/oceans/ncei/ocads/data/0237935/>. The mapped
1017 Argo-based fields of temperature and salinity are available at
1018 https://sio-argo.ucsd.edu/RG_Climatology.html. The WOA-mapped climatologies of
1019 silicic acid, nitrate, and dissolved oxygen are available at
1020 <https://www.nodc.noaa.gov/OC5/woa18/woa18data.html>. The atmospheric pCO₂

1021 based on the GlobalView xCO₂ is available at
 1022 https://www.nodc.noaa.gov/ocads/oceans/SPC02_1982_present_ETH_SOM_FFN.html.
 1023 The mapped annual climatology of DIC is available at
 1024 <https://www.ncei.noaa.gov/data/oceans/ncei/ocads/data/0162565/mapped/>. The
 1025 time-series data from HOT, BATS, and Drake Passage are available at
 1026 <http://hahana.soest.hawaii.edu/hot/hot-dogs/bextraction.html>,
 1027 <http://bats.bios.edu/bats-data/>, and
 1028 <https://www.nodc.noaa.gov/archive/arc0118/0171470/2.2/data/0-data/>,
 1029 respectively. The DIC estimated based on BGC-Argo floats in the Southern Ocean
 1030 (SOCCOM floats) is available at <http://socompu.princeton.edu/www/index.html>.
 1031 The OceanSODA surface DIC fields are available at [https://www.ncei.noaa.gov/](https://www.ncei.noaa.gov/access/metadata/landing-page/bin/iso?id=gov.noaa.nodc:0220059)
 1032 [access/metadata/landing-page/bin/iso?id=gov.noaa.nodc:0220059](https://www.ncei.noaa.gov/access/metadata/landing-page/bin/iso?id=gov.noaa.nodc:0220059). The
 1033 MOBO-DIC monthly climatology is available at [https://www.ncei.noaa.gov/access/](https://www.ncei.noaa.gov/access/metadata/landing-page/bin/iso?id=gov.noaa.nodc:0221526)
 1034 [metadata/landing-page/bin/iso?id=gov.noaa.nodc:0221526](https://www.ncei.noaa.gov/access/metadata/landing-page/bin/iso?id=gov.noaa.nodc:0221526). The monthly
 1035 climatology of DIC by Broulln et al. (2020) is available at
 1036 <https://doi.org/10.20350/digitalCSIC/10551>. The data for C_{ant} are available at
 1037 https://www.ncei.noaa.gov/access/ocean-carbon-data-system/oceans/ndp_100/
 1038 [ndp100.html](https://www.ncei.noaa.gov/access/ocean-carbon-data-system/oceans/ndp_100/) and [https://www.ncei.noaa.gov/access/metadata/landing-page/bin/](https://www.ncei.noaa.gov/access/metadata/landing-page/bin/iso?id=gov.noaa.nodc:0001644)
 1039 [iso?id=gov.noaa.nodc:0001644](https://www.ncei.noaa.gov/access/metadata/landing-page/bin/iso?id=gov.noaa.nodc:0001644) for the periods 1800 to 1994 and 1994 to 2007,
 1040 respectively. We use the bathymetry from Etopo2 (2001), and the Multivariate El Niño
 1041 Index (MEI; Wolter and Timlin (2011); <https://psl.noaa.gov/enso/mei/>).

1042 References

- 1043 Bakker, D. C. E., Pfeil, B., Landa, C. S., Metzl, N., O'Brien, K. M., Olsen, A., ... Xu, S.
 1044 (2016). A multi-decade record of high-quality fCO₂ data in version 3 of the Surface
 1045 Ocean CO₂ Atlas (SOCAT). *Earth System Science Data*, 8(2), 383–413. doi: 10.5194/
 1046 [essd-8-383-2016](https://doi.org/10.5194/essd-8-383-2016)
- 1047 Bates, N. R., Astor, Y. M., Church, M. J., Currie, K., Dore, J. E., Gonzalez-Davila,
 1048 M., ... Magdalena Santana-Casiano, J. (2014). A Time-Series View of Changing
 1049 Surface Ocean Chemistry Due to Ocean Uptake of Anthropogenic CO₂ and Ocean
 1050 Acidification. *Oceanography*, 27(1), 126–141. doi: 10.5670/oceanog.2014.16
- 1051 Bittig, H. C., Maurer, T. L., Plant, J. N., Schmechtig, C., Wong, A. P. S., Claustre, H.,
 1052 ... Xing, X. (2019). A BGC-Argo Guide: Planning, Deployment, Data Handling and
 1053 Usage. *Frontiers in Marine Science*, 6. doi: 10.3389/fmars.2019.00502
- 1054 Bittig, H. C., Steinhoff, T., Claustre, H., Fiedler, B., Williams, N. L., Sauzde, R., ...
 1055 Gattuso, J.-P. (2018). An Alternative to Static Climatologies: Robust Estimation of
 1056 Open Ocean CO₂ Variables and Nutrient Concentrations From T, S, and O₂ Data
 1057 Using Bayesian Neural Networks. *Frontiers in Marine Science*, 5. doi: 10.3389/
 1058 [fmars.2018.00328](https://doi.org/10.3389/fmars.2018.00328)
- 1059 Boyer, T. P., Garcia, H., Locarnini, R., Zweng, M., Mishonov, A. V., Reagan, J.,
 1060 ... Smolyar, I. (2018). *World Ocean Atlas 2018*. NOAA National Centers for
 1061 Environmental Information. Dataset. Retrieved from [https://www.ncei.noaa.gov/](https://www.ncei.noaa.gov/archive/accession/NCEI-WOA18)
 1062 [archive/accession/NCEI-WOA18](https://www.ncei.noaa.gov/archive/accession/NCEI-WOA18)
- 1063 Breeden, M. L., & McKinley, G. A. (2016). Climate impacts on multidecadal pCO₂
 1064 variability in the North Atlantic: 19482009. *Biogeosciences*, 13(11), 3387–3396. doi:
 1065 [10.5194/bg-13-3387-2016](https://doi.org/10.5194/bg-13-3387-2016)
- 1066 Brewer, P. G. (1978). Direct observation of the oceanic CO₂ increase. *Geophysical Research*
 1067 *Letters*, 5(12), 997–1000. doi: 10.1029/GL005i012p00997
- 1068 Broulln, D., Prez, F. F., Velo, A., Hoppema, M., Olsen, A., Takahashi, T., ... van Heuven,
 1069 S. M. A. C. (2019). A global monthly climatology of total alkalinity: a neural network
 1070 approach. *Earth System Science Data*, 11(3), 1109–1127. doi: 10.5194/essd-11-1109
 1071 -2019
- 1072 Broulln, D., Prez, F. F., Velo, A., Hoppema, M., Olsen, A., Takahashi, T., ... Kozyr, A.
 1073 (2020). A global monthly climatology of oceanic total dissolved inorganic carbon:

- 1074 a neural network approach. *Earth System Science Data*, *12*(3), 1725–1743. doi:
 1075 10.5194/essd-12-1725-2020
- 1076 Carter, B. R., Feely, R. A., Wanninkhof, R., Kouketsu, S., Sonnerup, R. E., Pardo, P. C.,
 1077 ... Bullister, J. L. (2019). Pacific Anthropogenic Carbon Between 1991 and 2017.
 1078 *Global Biogeochemical Cycles*, *33*(5), 597–617. doi: 10.1029/2018GB006154
- 1079 Carter, B. R., Feely, R. A., Williams, N. L., Dickson, A. G., Fong, M. B., & Takeshita, Y.
 1080 (2018). Updated methods for global locally interpolated estimation of alkalinity, pH,
 1081 and nitrate. *Limnology and Oceanography: Methods*, *16*(2), 119–131. doi: 10.1002/
 1082 lom3.10232
- 1083 Chen, G.-T., & Millero, F. J. (1979). Gradual increase of oceanic CO₂. *Nature*, *277*(5693),
 1084 205–206. doi: 10.1038/277205a0
- 1085 Cheng, L., Trenberth, K. E., Gruber, N., Abraham, J. P., Fasullo, J. T., Li, G., ... Zhu, J.
 1086 (2020). Improved Estimates of Changes in Upper Ocean Salinity and the Hydrological
 1087 Cycle. *American Meteorological Society Section: Journal of Climate*, *33*(23), 10357–
 1088 10381. doi: 10.1175/JCLI-D-20-0366.1
- 1089 Clement, D., & Gruber, N. (2018). The eMLR(C*) Method to Determine Decadal Changes
 1090 in the Global Ocean Storage of Anthropogenic CO₂. *Global Biogeochemical Cycles*,
 1091 *32*(4), 654–679. doi: 10.1002/2017GB005819
- 1092 DeVries, T., Holzer, M., & Primeau, F. (2017). Recent increase in oceanic carbon uptake
 1093 driven by weaker upper-ocean overturning. *Nature*, *542*(7640), 215–218. doi: 10.1038/
 1094 nature21068
- 1095 Doney, S. C., Fabry, V. J., Feely, R. A., & Kleypas, J. A. (2009). Ocean Acidification:
 1096 The Other CO₂ Problem. *Annual Review of Marine Science*, *1*(1), 169–192. doi:
 1097 10.1146/annurev.marine.010908.163834
- 1098 Dong, Y., Bakker, D. C. E., Bell, T. G., Huang, B., Landschtzer, P., Liss, P. S., &
 1099 Yang, M. (2022). Update on the Temperature Corrections of Global Air-Sea
 1100 CO₂ Flux Estimates. *Global Biogeochemical Cycles*, *36*(9), e2022GB007360. doi:
 1101 10.1029/2022GB007360
- 1102 Dore, J. E., Lukas, R., Sadler, D. W., Church, M. J., & Karl, D. M. (2009). Physical
 1103 and biogeochemical modulation of ocean acidification in the central North Pacific.
 1104 *Proceedings of the National Academy of Sciences of the United States of America*,
 1105 *106*(30), 12235–12240. doi: 10.1073/pnas.0906044106
- 1106 Etopo2. (2001). ETOPO2, Global 2 Arc-minute Ocean Depth and Land Elevation from
 1107 the US National Geophysical Data Center (NGDC). *National Geophysical Data
 1108 Center/NESDIS/NOAA/U.S. Department of Commerce*. (Research Data Archive
 1109 at the National Center for Atmospheric Research, Computational and Information
 1110 Systems Laboratory [dataset]) doi: 10.5065/D6668B75
- 1111 Fay, A. R., Gregor, L., Landschtzer, P., McKinley, G. A., Gruber, N., Gehlen, M., ...
 1112 Zeng, J. (2021). SeaFlux: harmonization of airsea CO₂ fluxes from surface pCO₂
 1113 data products using a standardized approach. *Earth System Science Data*, *13*(10),
 1114 4693–4710. doi: 10.5194/essd-13-4693-2021
- 1115 Fay, A. R., & McKinley, G. A. (2013). Global trends in surface ocean pCO₂ from in situ
 1116 data. *Global Biogeochemical Cycles*, *27*(2), 541–557. doi: 10.1002/gbc.20051
- 1117 Feely, R. A., Sabine, C. L., Lee, K., Berelson, W., Kleypas, J., Fabry, V. J., & Millero, F. J.
 1118 (2004). Impact of Anthropogenic CO₂ on the CaCO₃ System in the Oceans. *Science*,
 1119 *305*(5682), 362–366. doi: 10.1126/science.1097329
- 1120 Friedlingstein, P., Jones, M. W., O'Sullivan, M., Andrew, R. M., Bakker, D. C. E., Hauck,
 1121 J., ... Zeng, J. (2022). Global Carbon Budget 2021. *Earth System Science Data*,
 1122 *14*(4), 1917–2005. doi: 10.5194/essd-14-1917-2022
- 1123 Friis, K., Krtzinger, A., Ptsch, J., & Wallace, D. W. R. (2005). On the temporal increase
 1124 of anthropogenic CO₂ in the subpolar North Atlantic. *Deep Sea Research Part I:
 1125 Oceanographic Research Papers*, *52*(5), 681–698. doi: 10.1016/j.dsr.2004.11.017
- 1126 Friis, K., Krtzinger, A., & Wallace, D. W. R. (2003). The salinity normalization of marine
 1127 inorganic carbon chemistry data. *Geophysical Research Letters*, *30*(2). doi: 10.1029/
 1128 2002GL015898

- 1129 GlobalView-CO₂. (2011). *Cooperative Atmospheric Data Integration Project Carbon*
 1130 *Dioxide. Dataset*. Retrieved from <https://gml.noaa.gov/ccgg/globalview/>
- 1131 Gloege, L., McKinley, G. A., Landschutzer, P., Fay, A. R., Frlicher, T. L., Fyfe, J. C., ...
 1132 Takano, Y. (2021). Quantifying Errors in Observationally Based Estimates of Ocean
 1133 Carbon Sink Variability. *Global Biogeochemical Cycles*, *35*(4), e2020GB006788. doi:
 1134 10.1029/2020GB006788
- 1135 Gray, A. R., Johnson, K. S., Bushinsky, S. M., Riser, S. C., Russell, J. L., Talley, L. D., ...
 1136 Sarmiento, J. L. (2018). Autonomous biogeochemical floats detect significant carbon
 1137 dioxide outgassing in the high-latitude Southern Ocean. *Geophysical Research Letters*.
 1138 doi: 10.1029/2018GL078013
- 1139 Gregor, L., & Gruber, N. (2021). OceanSODA-ETHZ: a global gridded data set of the
 1140 surface ocean carbonate system for seasonal to decadal studies of ocean acidification.
 1141 *Earth System Science Data*, *13*(2), 777–808. doi: 10.5194/essd-13-777-2021
- 1142 Gregor, L., Kok, S., & Monteiro, P. M. S. (2017). Empirical methods for the estimation of
 1143 Southern Ocean CO₂: support vector and random forest regression. *Biogeosciences*,
 1144 *14*(23), 5551–5569. doi: 10.5194/bg-14-5551-2017
- 1145 Gruber, N. (1998). Anthropogenic CO₂ in the Atlantic Ocean. *Global Biogeochemical*
 1146 *Cycles*, *12*(1), 165–191. doi: 10.1029/97GB03658
- 1147 Gruber, N., Bakker, D. C. E., DeVries, T., Gregor, L., Hauck, J., Landschutzer, P., ...
 1148 Mueller, J. D. (2023). Trends and variability in the ocean carbon sink. *Nature*
 1149 *Reviews Earth and Environment*. doi: 10.1038/s43017-022-00381-x
- 1150 Gruber, N., Clement, D., Carter, B. R., Feely, R. A., Heuven, S. v., Hoppema, M., ...
 1151 Wanninkhof, R. (2019). The oceanic sink for anthropogenic CO₂ from 1994 to 2007.
 1152 *Science*, *363*(6432), 1193–1199. doi: 10.1126/science.aau5153
- 1153 Gruber, N., Gloor, M., Fletcher, S. E. M., Doney, S. C., Dutkiewicz, S., Follows, M. J.,
 1154 ... Takahashi, T. (2009). Oceanic sources, sinks, and transport of atmospheric CO₂.
 1155 *Global Biogeochemical Cycles*, *23*(1). doi: 10.1029/2008GB003349
- 1156 Gruber, N., Sarmiento, J. L., & Stocker, T. F. (1996). An improved method for detecting
 1157 anthropogenic CO₂ in the oceans. *Global Biogeochemical Cycles*, *10*(4), 809–837. doi:
 1158 10.1029/96GB01608
- 1159 Hauck, J., Vlker, C., Wang, T., Hoppema, M., Losch, M., & WolfGladrow, D. A. (2013).
 1160 Seasonally different carbon flux changes in the Southern Ocean in response to the
 1161 southern annular mode. *Global Biogeochemical Cycles*, *27*(4), 1236–1245. doi: 10
 1162 .1002/2013GB004600
- 1163 Hauck, J., Zeising, M., Le Qur, C., Gruber, N., Bakker, D. C. E., Bopp, L., ... Sfrjan, R.
 1164 (2020). Consistency and Challenges in the Ocean Carbon Sink Estimate for the Global
 1165 Carbon Budget. *Frontiers in Marine Science*, *7*, 852. doi: 10.3389/fmars.2020.571720
- 1166 Ilyina, T., Six, K. D., Segschneider, J., MaierReimer, E., Li, H., & NezRiboni, I. (2013).
 1167 Global ocean biogeochemistry model HAMOCC: Model architecture and performance
 1168 as component of the MPI-Earth system model in different CMIP5 experimental
 1169 realizations. *Journal of Advances in Modeling Earth Systems*, *5*(2), 287–315. doi:
 1170 10.1029/2012MS000178
- 1171 IPCC. (2021). *Climate Change 2021: The Physical Science Basis. Contribution of Working*
 1172 *Group I to the Sixth Assessment Report of the Intergovernmental Panel on Climate*
 1173 *Change* (V. Masson-Delmotte et al., Eds.). Cambridge University Press.
- 1174 Jacobson, A. R., Mikaloff Fletcher, S. E., Gruber, N., Sarmiento, J. L., & Gloor, M.
 1175 (2007). A joint atmosphere-ocean inversion for surface fluxes of carbon dioxide:
 1176 1. Methods and global-scale fluxes. *Global Biogeochemical Cycles*, *21*(1). doi:
 1177 10.1029/2005GB002556
- 1178 Joos, F., Plattner, G.-K., Stocker, T. F., Marchal, O., & Schmittner, A. (1999). Global
 1179 Warming and Marine Carbon Cycle Feedbacks on Future Atmospheric CO₂. *Science*,
 1180 *284*(5413), 464–467. doi: 10.1126/science.284.5413.464
- 1181 Keeling, R. (2005). Comment on "The Ocean Sink for Anthropogenic CO₂". *Science*,
 1182 *308*(5729), 1743c–1743c. doi: 10.1126/science.1109620
- 1183 Keppler, L., & Landschutzer, P. (2019). Regional Wind Variability Modulates the Southern

- 1184 Ocean Carbon Sink. *Scientific Reports*, 9(1), 1–10. doi: 10.1038/s41598-019-43826-y
- 1185 Keppler, L., Landschutzer, P., Gruber, N., Lauvset, S. K., & Stemmler, I. (2020a). Mapped
- 1186 Observation-Based Oceanic dissolved inorganic carbon (DIC), monthly climatology,
- 1187 from January to December (based on observations between 2004 and 2017), from
- 1188 the Max-Planck-Institute for Meteorology (MOBO-DIC_mpim). Dataset. *NOAA*
- 1189 *National Centers for Environmental Information, NCEI Accession 0221526*. Retrieved
- 1190 from [https://www.ncei.noaa.gov/access/metadata/landing-page/bin/iso?id=](https://www.ncei.noaa.gov/access/metadata/landing-page/bin/iso?id=gov.noaa.nodc%3A0221526)
- 1191 [gov.noaa.nodc%3A0221526](https://www.ncei.noaa.gov/access/metadata/landing-page/bin/iso?id=gov.noaa.nodc%3A0221526)
- 1192 Keppler, L., Landschutzer, P., Gruber, N., Lauvset, S. K., & Stemmler, I. (2020b). Seasonal
- 1193 Carbon Dynamics in the Near-Global Ocean. *Global Biogeochemical Cycles*, 34(12),
- 1194 e2020GB006571. doi: 10.1029/2020GB006571
- 1195 Kerr, R. A. (2000). A North Atlantic Climate Pacemaker for the Centuries. *Science*,
- 1196 288(5473), 1984–1985. doi: 10.1126/science.288.5473.1984
- 1197 Key, R. M., Kozyr, A., Sabine, C. L., Lee, K., Wanninkhof, R., Bullister, J. L., ...
- 1198 Peng, T.-H. (2004). A global ocean carbon climatology: Results from Global
- 1199 Data Analysis Project (GLODAP). *Global Biogeochemical Cycles*, 18(4). doi:
- 1200 10.1029/2004GB002247
- 1201 Lacroix, F., Ilyina, T., & Hartmann, J. (2020). Oceanic CO₂ outgassing and biological
- 1202 production hotspots induced by pre-industrial river loads of nutrients and carbon in a
- 1203 global modeling approach. *Biogeosciences*, 17(1), 55–88. doi: 10.5194/bg-17-55-2020
- 1204 Landschutzer, P., Gruber, N., & Bakker, D. C. E. (2016). Decadal variations and trends of
- 1205 the global ocean carbon sink. *Global Biogeochemical Cycles*, 30(10), 1396–1417. doi:
- 1206 10.1002/2015GB005359
- 1207 Landschutzer, P., Gruber, N., Bakker, D. C. E., & Schuster, U. (2014). Recent variability
- 1208 of the global ocean carbon sink. *Global Biogeochemical Cycles*, 28(9), 927–949. doi:
- 1209 10.1002/2014GB004853
- 1210 Landschutzer, P., Gruber, N., Bakker, D. C. E., Schuster, U., Nakaoka, S., Payne, M. R.,
- 1211 ... Zeng, J. (2013). A neural network-based estimate of the seasonal to inter-annual
- 1212 variability of the Atlantic Ocean carbon sink. *Biogeosciences*, 10(11), 7793–7815. doi:
- 1213 10.5194/bg-10-7793-2013
- 1214 Landschutzer, P., Gruber, N., Haumann, A., Rdenbeck, C., Bakker, D. C. E., van Heuven,
- 1215 S., ... Wanninkhof, R. (2015). The reinvigoration of the Southern Ocean carbon sink.
- 1216 *Science*, 349(6253), 1221–1224. doi: 10.1126/science.aab2620
- 1217 Landschutzer, P., Keppler, L., & Ilyina, T. (2022). Chapter 13: Ocean Systems. In *Balancing*
- 1218 *Greenhouse Gas Budgets - Accounting for Natural and Anthropogenic Flows of CO₂*
- 1219 *and other Trace Gases* (1st ed.). Elsevier.
- 1220 Lauvset, S. K., Key, R. M., Olsen, A., van Heuven, S., Velo, A., Lin, X., ... Watelet, S.
- 1221 (2016). A new global interior ocean mapped climatology: the 1 1 GLODAP version
- 1222 2. *Earth System Science Data*, 8(2), 325–340. doi: 10.5194/essd-8-325-2016
- 1223 Lauvset, S. K., Lange, N., Tanhua, T., Bittig, H. C., Olsen, A., Kozyr, A., ... Key, R. M.
- 1224 (2021). An updated version of the global interior ocean biogeochemical data product,
- 1225 GLODAPv2.2021. *Earth System Science Data*, 13(12), 5565–5589. doi: 10.5194/
- 1226 essd-13-5565-2021
- 1227 Lenton, A., & Matear, R. J. (2007). Role of the Southern Annular Mode (SAM) in Southern
- 1228 Ocean CO₂ uptake. *Global Biogeochemical Cycles*, 21(2), GB2016. doi: 10.1029/
- 1229 2006GB002714
- 1230 Le Qur, C., Rdenbeck, C., Buitenhuis, E. T., Conway, T. J., Langenfelds, R., Gomez, A.,
- 1231 ... Heimann, M. (2007). Saturation of the Southern Ocean CO₂ sink due to recent
- 1232 climate change. *Science*, 316(5832), 1735–1738. doi: 10.1126/science.1136188
- 1233 Lovenduski, N. S., Gruber, N., & Doney, S. C. (2008). Toward a mechanistic understanding
- 1234 of the decadal trends in the Southern Ocean carbon sink. *Global Biogeochemical*
- 1235 *Cycles*, 22(3), GB3016. doi: 10.1029/2007GB003139
- 1236 Lovenduski, N. S., Gruber, N., Doney, S. C., & Lima, I. D. (2007). Enhanced CO₂ outgassing
- 1237 in the Southern Ocean from a positive phase of the Southern Annular Mode. *Global*
- 1238 *Biogeochemical Cycles*, 21(2), GB2026. doi: 10.1029/2006GB002900

- 1239 Mantua, N. J., & Hare, S. R. (2002). The Pacific Decadal Oscillation. *Journal of*
 1240 *Oceanography*, *58*(1), 35–44. doi: 10.1023/A:1015820616384
- 1241 Matear, R. J., & Hirst, A. C. (1999). Climate change feedback on the future oceanic
 1242 CO₂ uptake. *Tellus B: Chemical and Physical Meteorology*, *51*(3), 722–733. doi:
 1243 10.3402/tellusb.v51i3.16472
- 1244 Matsumoto, K., & Gruber, N. (2005). How accurate is the estimation of anthropogenic
 1245 carbon in the ocean? An evaluation of the DeltaC* method. *Global Biogeochemical*
 1246 *Cycles*, *19*(3). doi: 10.1029/2004GB002397
- 1247 Mauritsen, T., Bader, J., Becker, T., Behrens, J., Bittner, M., Brokopf, R., . . . Roeckner, E.
 1248 (2019). Developments in the MPI-M Earth System Model version 1.2 (MPI-ESM1.2)
 1249 and Its Response to Increasing CO₂. *Journal of Advances in Modeling Earth Systems*,
 1250 *11*(4), 998–1038. doi: 10.1029/2018MS001400
- 1251 McKinley, G. A., Fay, A. R., Eddebbar, Y. A., Gloege, L., & Lovenduski, N. S. (2020).
 1252 External Forcing Explains Recent Decadal Variability of the Ocean Carbon Sink. *AGU*
 1253 *Advances*, *1*(2), e2019AV000149. doi: 10.1029/2019AV000149
- 1254 McNeil, B. I., & Matear, R. J. (2013). The non-steady state oceanic CO₂ signal: its
 1255 importance, magnitude and a novel way to detect it. *Biogeosciences*, *10*(4), 2219–
 1256 2228. doi: 10.5194/bg-10-2219-2013
- 1257 McNeil, B. I., & Sasse, T. P. (2016). Future ocean hypercapnia driven by anthropogenic
 1258 amplification of the natural CO₂ cycle. *Nature*, *529*(7586), 383–386. doi: 10.1038/
 1259 nature16156
- 1260 Mikaloff Fletcher, S. E. M., Gruber, N., Jacobson, A. R., Doney, S. C., Dutkiewicz, S.,
 1261 Gerber, M., . . . Sarmiento, J. L. (2006). Inverse estimates of anthropogenic CO₂
 1262 uptake, transport, and storage by the ocean. *Global Biogeochemical Cycles*, *20*(2),
 1263 GB2002. doi: 10.1029/2005GB002530
- 1264 Olsen, A., Key, R. M., Heuven, S. v., Lauvset, S. K., Velo, A., Lin, X., . . . Suzuki, T.
 1265 (2016). The Global Ocean Data Analysis Project version 2 (GLODAPv2) an internally
 1266 consistent data product for the world ocean. *Earth System Science Data*, *8*(2), 297–
 1267 323. doi: 10.5194/essd-8-297-2016
- 1268 Orr, J. C., Fabry, V. J., Aumont, O., Bopp, L., Doney, S. C., Feely, R. A., . . . Yool, A.
 1269 (2005). Anthropogenic ocean acidification over the twenty-first century and its impact
 1270 on calcifying organisms. *Nature*, *437*(7059), 681–686. doi: 10.1038/nature04095
- 1271 Rdenbeck, C., Bakker, D. C. E., Gruber, N., Iida, Y., Jacobson, A. R., Jones, S., . . . Zeng, J.
 1272 (2015). Data-based estimates of the ocean carbon sink variability first results of the
 1273 Surface Ocean pCO₂ Mapping intercomparison (SOCOM). *Biogeosciences*, *12*(23),
 1274 7251–7278. doi: 10.5194/bg-12-7251-2015
- 1275 Regnier, P., Resplandy, L., Najjar, R. G., & Ciais, P. (2022). The land-to-ocean loops of the
 1276 global carbon cycle. *Nature*, *603*(7901), 401–410. doi: 10.1038/s41586-021-04339-9
- 1277 Resplandy, L., Keeling, R. F., Rdenbeck, C., Stephens, B. B., Khatiwala, S., Rodgers, K. B.,
 1278 . . . Tans, P. P. (2018). Revision of global carbon fluxes based on a reassessment of
 1279 oceanic and riverine carbon transport. *Nature Geoscience*, *1*. doi: 10.1038/s41561-018-
 1280 -0151-3
- 1281 Roemmich, D., & Gilson, J. (2009). The 2004–2008 mean and annual cycle of temperature,
 1282 salinity, and steric height in the global ocean from the Argo Program. *Progress in*
 1283 *Oceanography*, *82*(2), 81–100. doi: 10.1016/j.pocean.2009.03.004
- 1284 Roobaert, A., Laruelle, G. G., Landschutzer, P., Gruber, N., Chou, L., & Regnier, P.
 1285 (2019). The Spatiotemporal Dynamics of the Sources and Sinks of CO₂ in the
 1286 Global Coastal Ocean. *Global Biogeochemical Cycles*, *33*(12), 1693–1714. doi:
 1287 10.1029/2019GB006239
- 1288 Sabine, C. L., Feely, R. A., Gruber, N., Key, R. M., Lee, K., Bullister, J. L., . . . Rios, A. F.
 1289 (2004). The oceanic sink for anthropogenic CO₂. *Science*, *305*(5682), 367–371. doi:
 1290 10.1126/science.1097403
- 1291 Sabine, C. L., & Gruber, N. (2005). Response to Comment on "The Ocean Sink for
 1292 Anthropogenic CO₂". *Science*, *308*(5729), 1743–1743. doi: 10.1126/science.1109949
- 1293 Sabine, C. L., Key, R. M., Johnson, K. M., Millero, F. J., Poisson, A., Sarmiento, J. L.,

- 1294 ... Winn, C. D. (1999). Anthropogenic CO₂ inventory of the Indian Ocean. *Global*
1295 *Biogeochemical Cycles*, 13(1), 179–198. doi: 10.1029/1998GB900022
- 1296 Sarmiento, J. L., & Gruber, N. (2002). Sinks for Anthropogenic Carbon. *Physics Today*,
1297 55(8), 30–36. doi: 10.1063/1.1510279
- 1298 Sarmiento, J. L., & Gruber, N. (2006). Carbon Cycle, CO₂, and Climate; the Anthropogenic
1299 Perturbation. In *Ocean Biogeochemical Dynamics* (pp. 399–417). Princeton University
1300 Press.
- 1301 Sarmiento, J. L., Hughes, T. M. C., Stouffer, R. J., & Manabe, S. (1998). Simulated response
1302 of the ocean carbon cycle to anthropogenic climate warming. *Nature*, 393(6682), 245–
1303 249. doi: 10.1038/30455
- 1304 Sarmiento, J. L., Le Qur, C., & Pacala, S. W. (1995). Limiting future atmospheric carbon
1305 dioxide. *Global Biogeochemical Cycles*, 9(1), 121–137. doi: 10.1029/94GB01779
- 1306 Sarmiento, J. L., & Sundquist, E. T. (1992). Revised budget for the oceanic uptake of
1307 anthropogenic carbon dioxide. *Nature*, 356(6370), 589–593. doi: 10.1038/356589a0
- 1308 Sasse, T. P., McNeil, B. I., & Abramowitz, G. (2013). A novel method for diagnosing
1309 seasonal to inter-annual surface ocean carbon dynamics from bottle data using neural
1310 networks. *Biogeosciences*, 10(6), 4319–4340. doi: 10.5194/bg-10-4319-2013
- 1311 Sharp, J. D., Fassbender, A. J., Carter, B. R., Johnson, G. C., Schultz, C., & Dunne, J. P.
1312 (2022). GOBAI-O₂: temporally and spatially resolved fields of ocean interior dissolved
1313 oxygen over nearly two decades. *Earth System Science Data Discussions*, 1–46. doi:
1314 10.5194/essd-2022-308
- 1315 Talley, L., Feely, R., Sloyan, B., Wanninkhof, R., Baringer, M., Bullister, J., ... Zhang,
1316 J.-Z. (2016). Changes in Ocean Heat, Carbon Content, and Ventilation: A Review of
1317 the First Decade of GO-SHIP Global Repeat Hydrography. *Annual Review of Marine*
1318 *Science*, 8(1), 185–215. doi: 10.1146/annurev-marine-052915-100829
- 1319 Talley, L., Rosso, I., Kamenkovich, I., Mazloff, M. R., Wang, J., Boss, E., ... Sarmiento,
1320 J. L. (2019). Southern Ocean Biogeochemical Float Deployment Strategy, With
1321 Example From the Greenwich Meridian Line (GO-SHIP A12). *Journal of Geophysical*
1322 *Research: Oceans*, 124(1), 403–431. doi: 10.1029/2018JC014059
- 1323 Tanhua, T., Krtzinger, A., Friis, K., Waugh, D. W., & Wallace, D. W. R. (2007). An
1324 estimate of anthropogenic CO₂ inventory from decadal changes in oceanic carbon
1325 content. *Proceedings of the National Academy of Sciences*, 104(9), 3037–3042. doi:
1326 10.1073/pnas.0606574104
- 1327 Terhaar, J., Flicher, T. L., & Joos, F. (2022). Observation-constrained estimates of the
1328 global ocean carbon sink from Earth System Models. *Biogeosciences Discussions*,
1329 1–49. doi: 10.5194/bg-2022-134
- 1330 Torres, O., Kwiatkowski, L., Sutton, A. J., Dorey, N., & Orr, J. C. (2021). Characterizing
1331 Mean and Extreme Diurnal Variability of Ocean CO₂ System Variables Across Marine
1332 Environments. *Geophysical Research Letters*, 48(5), e2020GL090228. doi: 10.1029/
1333 2020GL090228
- 1334 Turner, K. E., Smith, D. M., Katavouta, A., & Williams, R. G. (2022). Reconstructing ocean
1335 carbon storage with CMIP6 models and synthetic Argo observations. *Biogeosciences*
1336 *Discussions*, 1–29. doi: 10.5194/bg-2022-166
- 1337 van Heuven, S., Pierrot, D., Rae, J., Lewis, E., & Wallace, D. (2011). *MATLAB Program*
1338 *Developed for CO₂ System Calculations*. Oak Ridge, Tennessee: ORNL/CDIAC-105b.
1339 Carbon Dioxide Information Analysis Center, Oak Ridge National Laboratory, U.S.
1340 Department of Energy,.
- 1341 Wallace, D. W. (1995). Monitoring global ocean carbon inventories. In *Scientific Design for*
1342 *the Common Module of the Global Ocean Observing System and the Global Climate*
1343 *Observing System: An Ocean Observing System for Climate : Final Report of the*
1344 *Ocean Observing System Development Panel*. Texas A&M University.
- 1345 Wanninkhof, R., Asher, W. E., Ho, D. T., Sweeney, C., & McGillis, W. R. (2009). Advances
1346 in Quantifying Air-Sea Gas Exchange and Environmental Forcing. *Annual Review of*
1347 *Marine Science*, 1(1), 213–244. doi: 10.1146/annurev.marine.010908.163742
- 1348 Wanninkhof, R., Doney, S. C., Bullister, J. L., Levine, N. M., Warner, M., & Gruber,

1349 N. (2010). Detecting anthropogenic CO₂ changes in the interior Atlantic Ocean
1350 between 1989 and 2005. *Journal of Geophysical Research: Oceans*, 115(C11). doi:
1351 10.1029/2010JC006251

1352 Watson, A. J., Schuster, U., Shutler, J. D., Holding, T., Ashton, I. G. C., Landschtzer, P.,
1353 ... Goddijn-Murphy, L. (2020). Revised estimates of ocean-atmosphere CO₂ flux are
1354 consistent with ocean carbon inventory. *Nature Communications*, 11(1), 4422. doi:
1355 10.1038/s41467-020-18203-3

1356 Wolter, K., & Timlin, M. S. (2011). El Nio/Southern Oscillation behaviour since 1871 as
1357 diagnosed in an extended multivariate ENSO index (MEI.ext). *International Journal*
1358 *of Climatology*, 31(7), 1074–1087. doi: 10.1002/joc.2336

1359 Zickfeld, K., Fyfe, J. C., Saenko, O. A., Eby, M., & Weaver, A. J. (2007). Response of
1360 the global carbon cycle to human-induced changes in Southern Hemisphere winds.
1361 *Geophysical Research Letters*, 34(12). doi: 10.1029/2006GL028797